ABSTRACT

Title of Dissertation: HIGH THROUGHPUT STIMULATED BRILLOUIN SCATTERING SPECTROSCOPY

Jake Robert Rosvold,
Doctor of Philosophy, 2024

Dissertation directed by: Professor, Giuliano Scarcelli,
Fischell Department of Bioengineering

Brillouin light scattering arises from the coupled interaction between light and material acoustic phonons. The measurand of Brillouin scattering is the characteristic frequency difference between incident and scattered light which depends on the local longitudinal modulus of the material. Spontaneous Brillouin scattering has been used in combination with confocal microscopy to provide non-contact, label-free mapping at micron-scale resolution in biological media. To date, spontaneous Brillouin microscopy has reached the speed limit (~20-50ms per spectrum) as determined by the theoretical scattering efficiency. While a great deal of research has been directed to speeding up Brillouin microscopy acquisition times, spontaneous Brillouin scattering is fundamentally an inefficient process thus limiting the ability to study faster biological phenomena and rapid processes. To combat this limitation, its nonlinear counterpart, stimulated Brillouin scattering (SBS) has been proposed for microscopy applications. For decades, stimulated Brillouin scattering has been used in fiber sensing and all-optical pulse control and leverages a nonlinear interaction where two counterpropagating light beams

stimulate a more efficient scattering relationship. However, the small interaction volumes and photodamage constraints presented in microscopy have hindered the translation of stimulated Brillouin scattering into the biological realm. Recently, continuous wave stimulated Brillouin microscopy has led to competitive acquisition times (~5ms per spectrum) when compared to the spontaneous alternative but has yet to be widely adopted. Due to a plethora of factors, such as an inefficient power balance between pump and probe beams, lack of proper commercial laser sources, and nonoptimal detection schemes, the complete picture of what SBS spectroscopy has to offer has yet to be revealed. As such, there is a need to customize light sources and detection schemes in order to fully take advantage of the enhanced Brillouin efficiency possible in SBS.

Herein we introduce novel methodology to improve the acquisition speed of Brillouin microscopy by designing and developing proper laser sources and detection schemes for efficient SBS spectroscopy. First, we showcase the potential utility of our state-of-the-art continuous wave SBS technology in a flow cytometry application, highly suitable for the counterpropagating geometry of SBS where the laser position is fixed while the sample is being moved at high speeds. Additionally, we will present an optimized receiver design based on polarization detection which enables 100x faster spectral measurements in the low-gain regime relevant to biological materials. Finally, we demonstrate an optimal pulsed laser source specifically designed for SBS Brillouin microscopy.

HIGH THROUGHPUT STIMULATED BRILLOUIN SCATTERING SPECTROSCOPY

by

Jake Robert Rosvold

Dissertation submitted to the Faculty of the Graduate School of the
University of Maryland, College Park, in partial fulfillment
of the requirements for the degree of
Doctor of Philosophy
2024

Advisory Committee:
Professor Giuliano Scarcelli, Chair
Professor Jenna Mueller
Professor Thomas Murphy
Professor Yang Tao
Professor Ian White

Dedication

To my friends and family
My work is not yet done
Why wait?
JRR

Acknowledgements

I had no idea at the beginning of graduate school that I would learn just as much about people as I would about science and technology. In fact, I would wager maybe a bit more on the former. For that, I owe an incredible amount of thanks to my adviser, Giuliano Scarcelli. From day one of being in Maryland I felt a respect and level of confidence from him that I had seldom come across before. I have no doubt that the lessons I have learned from him will carry far beyond graduate school and have shaped me into a person I am proud to be. Giuliano takes time to learn what motivates his students and that is reflected in many ways. Whether he was outing me for being a 'capitalist' in the NSF ICORPS program or being my coach and giving me a Baltimore Ravens style half-time pep talk or giving infamous lab meeting speeches about America, he was always in my corner and cared.

I have been blessed with the absolute best lab mates and cherish each and every one of them: Giulia Zanini, Yogeshwari Ambekar, Jiarui Li, Maggie Zhou, Raymundo Rodríguez-López, Chenchen Handler, Romanus Hutchins, Eric Frank, Justin Schumacher, Theo Gifford and Ivano D'Alessandro. Each of them are very special to me and I consider myself lucky to have met them all.

I would not be the scientist I am today without the guidance of Giulia Zanini. She was an incredible influence on me, and I hope she realizes just how much the time I spent under her guidance meant to me. I also appreciate the Italian lessons when experiments were going poorly. To Romanus Hutchins and Justin Schumacher, the amount of money we spent on Vigilante Coffee trips pales in comparison to the value of our friendship. This is only the beginning of

‘The Three Musketeers’ and I look forward to watching us push onwards and upwards. You both are incredibly talented and worthy of the successes I know are in your futures.

I could not have accomplished what I have without the vast wisdom and support from both Brandon Redding and Joe Murray. The mentorship I received from you both is invaluable. To my committee I extend my very heartfelt gratitude towards their academic guidance and advisement.

Last but certainly not least, my family. You have all seen *me*; the person I was, the person I am, and the person I have yet to become. While I stumble along trying to find my path in life, you have all been there to cast the light forward. To my parents, Jill and Bob Rosvold, who have sacrificed everything for me and my siblings, you both inspire me on a daily basis to be the best that I can be, and you have shown me what it means to love someone. To my brother and sister, Carly and Luke Rosvold, who have been my absolute best friends since day one, I cannot imagine my life without you both. From being homeschooled together to becoming fellow Terps, I am so proud to watch your growth and successes. To the rest of my family, I was told at a young age to “shoot for the stars” and that is something I strive to do every day to make you all proud.

Table of Contents

List of Figures

List of Abbreviations

^{85}Rb:	Rubidium-85
AOM:	Acousto-optic modulator
ASD:	Amplitude spectral density
ASE:	Amplified spontaneous emission
CW:	Continuous wave
DSB-SC:	Double sideband suppressed carrier
EDFA:	Erbium doped fiber amplifier
FBG:	Fiber bragg grating
FP:	Fabry-Perot
FWHM:	Full-width at half maximum
LIA:	Lock-in amplifier
MOPA:	Master oscillator power amplifier
PRF:	Pulse repetition frequency
PSF:	Point spread function
RF:	Radio frequency
SBS:	Stimulated Brillouin scattering
SNR:	Signal-to-noise ratio
VIPA:	Virtually imaged phased array

Chapter 1: Introduction

1.1 Spontaneous Brillouin scattering microscopy

1.1.1 Spontaneous Brillouin scattering

When light travels in a medium, it has a chance of spontaneously scattering as a result of various fluctuations in the material's optical properties; these fluctuations can be caused by a number of physical processes which can impact the resultant parameters of the scattered light such as frequency shift and linewidth. For example, light scattering can occur due to the interaction of light with the vibrational modes of molecules (Raman), from propagating pressure waves (Brillouin), from nonpropagating density fluctuations (Rayleigh-center), or from fluctuations in the orientations of anisotropic molecules (Rayleigh-wing).

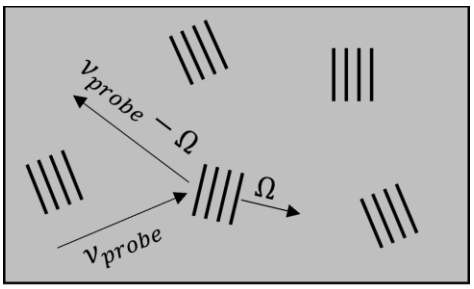

Fig. 1.1. Schematic illustrating the spontaneous (Stokes) Brillouin scattering process.

For the purposes of this chapter, we will focus on the Brillouin scattering phenomena which characteristically couples optical photons with acoustic phonons traveling intrinsically in the material[1]. Brillouin scattering was first introduced in 1922 [1] and first experimentally demonstrated in 1930 [2]. The interaction between the acoustic phonons and the optical photons results in an energy exchange, see Fig 1.1, based on the local longitudinal modulus, that can be observed as a frequency shift of the scattered light. Depending on whether the incident photons gained (Stokes) or lost energy (Anti-stokes) in the exchange, the frequency of the scattered light will be shifted down or up by the frequency of the phonon (Ω) with respect to the initial probe frequency (ν_{probe}). This relationship can be described as:

$$\Omega = \nu_{probe} \pm \nu_B \tag{1.1}$$

Where ν_B is the Brillouin shift associated with the Brillouin scattering phenomenon. The thermal acoustic phonons traveling through the material ($\Omega = |\boldsymbol{q}|v_s$ where v_s is the propagating speed of the sound wave, $|\boldsymbol{q}| = 2|\boldsymbol{k}| \sin\left(\frac{\theta}{2}\right)$ is the phonon wavevector and θ is the angle between the scattered and incident wavevectors) interact in a scattering event with the incident photons traveling in the material ($|\boldsymbol{k}| = \frac{\nu_{probe} * n}{c}$ where $|\boldsymbol{k}|$ defines the incident light's wavevector, n is the index of refraction, and c is the speed of light). The scattered light, whose frequency is given by conservation of energy and momentum ($|\boldsymbol{k}'| =$

[1] These acoustic phonons are intrinsic to the media insofar as they are spontaneously, thermally generated; in the next section, we will discuss the stimulated version of this process where the phonons are the result of high intensity light fields.

$|\boldsymbol{k}| \pm |\boldsymbol{q}|$ where $|\boldsymbol{k}'|$ defines the scattered light's wavevector), leads to the definition of the characteristic Brillouin shift.

$$\nu_B = 2n\frac{\nu_{probe}}{c}\nu_s \sin\left(\frac{\theta}{2}\right) = 2n\frac{\nu_{probe}}{c}\sqrt{\frac{M'}{\rho}}\sin\left(\frac{\theta}{2}\right) \tag{1.2}$$

Where ρ is the density and M' is the real part of the complex longitudinal modulus ($M = M' + iM''$). Thus, in solid materials, the longitudinal modulus is the uniaxial stress-strain ratio at frequency ν_B, thus $\nu_B \propto \sqrt{M'}$. We will revisit this concept in Chapter 2.

1.1.2 Spontaneous Brillouin instrumentation

Since the acoustic wave frequency is much smaller than the frequency of the light, this Brillouin shift can be on the order of 1-10 GHz, posing a need for spectrometers with high resolution and high spectral extinction to reject the back reflected probe light. Take water as an example; water has a Brillouin shift of ~5GHz at 780nm which is wavelength shift of ~0.005nm. Traditional filters or dispersive elements such as gratings do not have the spectral resolution, nor the extinction required to visualize the Brillouin phenomenon. Notwithstanding, this spontaneous process is also quite weak as the scattering efficiency is independent of the probe power[2] meaning high throughput is also a requirement of spontaneous Brillouin spectrometers.

In the 1970s, the first spectrometers capable of providing the high spectral *and* high extinction required to acquire Brillouin scattered photons were developed [3]. The

[2] The ideal total Brillouin scattered optical power is $\approx 10^{-11} P_{probe}$ in water.

technology featured a Fabry-Pérot (FP) etalon which is comprised of two partially reflective mirrors with a controlled cavity length that determines the transmission of the FP cavity. By scanning the cavity length, the Brillouin spectrum could be analyzed with sufficient spectral extinction when operated in double-pass (60dB). Roughly ten years later, the first demonstration of Brillouin measurements in biologically relevant materials was conducted; the researchers characterized the mechanical properties of the lens and cornea [4,5]. However, the high spectral resolution and extinction came at a cost because the FP etalons used in early adaptations of Brillouin spectroscopy suffered from low transmission which in turn made measurement times on the order of minutes to hours for a single spectral sweep. For obvious reasons, these measurement times severely limited the use of Brillouin spectroscopy for biological research purposes.

For more than 20 years, Brillouin spectroscopy research in the biological context was held stagnant until 2008 when Scarcelli and Yun [6] provided a critical solution to the FP etalon drawbacks. They adopted a relatively new kind of spectroscopic technique that leveraged virtually imaged phase arrays (VIPAs) which are very similar in nature to FP etalons, but have a totally reflective front surface with a small transparent window and a partially reflective back surface [7]. The VIPAs featured much higher throughput and when tilted at an angle, constructive interference separated the spectral features of the input light in space, making the use of VIPAs for Brillouin spectroscopy single shot – no cavity scanning required. Multi-stage VIPA configurations [8,9] led to further improvements of the spectral extinction albeit with significantly higher throughput compared to FP etalon

iterations. This breakthrough brought spectral measurement time down to 100ms per spectrum and finally made Brillouin-based microscopy a conceivable idea.

1.1.3 Spontaneous Brillouin scattering in microscopy

VIPA-based Brillouin spectrometers were implemented with confocal microscopy as a way to all-optically probe the material mechanical properties. Since, as previously stated, the measured Brillouin frequency shift is related to the speed of sound in the material, Brillouin spectroscopy probes the local longitudinal modulus of the material. More specifically, the Brillouin shift is related to the longitudinal modulus by ($\nu_B \propto \sqrt{M'}$, see Eq. 1.2). As such, Brillouin measurements extract the mechanical information of the material and an empirical relationship between the real part of the complex longitudinal modulus (M') and the more widely measured Young's modulus (E') has been shown in biological samples previously [10–12]. Since its introduction, spontaneous Brillouin scattering microscopy has become widely adopted to measure all sorts of biological materials: the cornea [11,12], chick embryo [13], and intra-cellular processes [10,14,15] just to name a few instances.

Prior to the development of more sophisticated spectrometer design, Brillouin spectroscopy with respect to biological materials was sparsely used because of the stringent requirements of high spectral resolution and high extinction that, at the time, only FP etalons could satisfy. Once VIPAs were introduced and significant speed improvements were achieved, the spectral acquisition times associated with spontaneous Brillouin scattering microscopes began to reach a fundamental limit. To date, spontaneous Brillouin

scattering microscopes have achieved at best ~50ms spectral acquisition times, i.e. the time to acquire one Brillouin spectrum, in biological samples and ~20ms in liquids [16,17] in point-sample configurations. This is in part due to the fundamental limitation imparted by the scattering efficiency, i.e. the ratio of the power of the scattered and incident light, of the spontaneous process being on the order of $10^{-10} - 10^{-11}$ in typical biological samples [18]. The use of high power lasers to compensate for this weak signal is bounded by the photodamage constraints introduced in the measurement of biological samples, namely thermal damage due to unwanted absorption of incident light [19,20]. How this presents with respect to achievable signal-to-noise ratios (SNRs) will be explored in greater detail in Chapter 3.

1.2 Stimulated Brillouin scattering microscopy

1.2.1 Nonlinear light-matter interactions

We will begin by introducing the concept of polarization, that is to say, the dipole moment per unit volume, of a material system which is dependent on the electric field strength of various incident optical field or fields. The polarization can be expressed by the following power series [21]:

$$\tilde{P}(t) = \epsilon_0\left[\chi^{(1)}\tilde{E}(t) + \chi^{(2)}\tilde{E}^2(t) + \chi^{(3)}\tilde{E}^3(t) + \cdots\right] \qquad (1.3)$$

Where $\tilde{P}$ is the material polarization, ϵ_0 is the electric permittivity of free space, $\chi^{(n)}$ is the electric susceptibility of order n (which is a tensor of rank $n+1$), and $\tilde{E}$ is the applied electric field. The various terms of this expression can be broken down to understand the

many processes that can occur in materials when under an applied electric field. For example, first-order nonlinear polarization ($\tilde{P}^{(1)}(t) = \epsilon_0 \chi^{(1)} \tilde{E}(t)$), which somewhat seems like a humorous misnomer, refers to *linear* optical phenomena under weak applied electric fields. These properties are constant, and their signals are proportional to the incident light intensity. Some examples of these are single photon absorption, reflection, and spontaneous scattering events. Spontaneous Brillouin scattering falls under this categorization. Second-order nonlinear polarization, for the purposes of this thesis, are uninteresting as for the materials we are concerned with, e.g. liquids and glass, cannot exhibit nonlinear optical effects of this order due to inversion symmetry. Which leads us to third-order nonlinear optical phenomena, most of which are out of scope (the Kerr effect, multiphoton absorption, etc.) but does include the topic of nonlinear frequency conversion. Stimulated Brillouin scattering is a prime example of this.

SBS is the result of a coupling between optical and acoustical waves. For the purposes of this thesis, we will be considering longitudinal acoustic modes rather than shear acoustic modes. Shear acoustic modes are the result of flexural, radial-axial, torsional acoustic vibrations which present at different frequencies than longitudinal modes due to the differing phase-matching conditions. To analyze the nonlinear relationship, first we ought to describe the various waves involved. Firstly, the light fields are considered:

$$\tilde{E}(z,t) = \tilde{E}_{pump}(z,t) + \tilde{E}_{probe}(z,t) \tag{1.4}$$

Where $\tilde{E}$ is the total electrical field.

$$\tilde{E}_{pump}(z,t) = A_{pump}(z,t) e^{i(k_{pump} z - 2\pi \nu_{pump} t)} + c.c. \tag{1.5}$$

$$\tilde{E}_{probe}(z,t) = A_{probe}(z,t)e^{i(-k_{probe}z-2\pi\nu_{probe}t)} + c.c. \quad (1.6)$$

Where A is the electric field amplitude. Notice that the probe electric field is traveling in the negative z-direction as opposed to the pump electric field[3]. The local compression of the material in response to the electric field strength will cause molecules to congregate in high electric field regions, which increases the local density and changes the refractive index via electrostriction. This can be described in terms of the acoustic field by:

$$\tilde{\rho}(z,t) = \rho_0 + \Delta\rho = \rho_0 + \rho(z,t)e^{i(qz-\Omega t)} + c.c. \quad (1.7)$$

Where Ω is the phonon frequency, q is the wavevector of the phonon, and ρ_0 is the average material density. The second term on the right side of the equation provides an expression of the time dependent change in density. This change in material density satisfies the acoustic wave equation:

$$\frac{\partial^2\tilde{\rho}}{\partial t^2} - \Gamma'\nabla^2\frac{\partial\tilde{\rho}}{\partial t} - v_s^2\nabla^2\tilde{\rho} = -\nabla\cdot\boldsymbol{F} \quad (1.8)$$

Where Γ' is the damping parameter and $\boldsymbol{F}$ is the electric field force originating from electrostriction pressure determined by considering how the light field energy density changes (ΔW) relate to the electrostriction pressure [22]:

$$\Delta W = \frac{1}{2}\Delta\epsilon\langle\tilde{E}^2\rangle = \frac{1}{2}\left(\frac{\partial\epsilon}{\partial\rho}\Delta\rho\right)\langle\tilde{E}^2\rangle = \frac{1}{2}\left(\gamma_e\frac{\Delta\rho}{\rho}\right)\langle\tilde{E}^2\rangle \quad (1.9)$$

Where $\langle\tilde{E}^2\rangle$ is the average intensity of the light field. This again calls out the importance of high intensity light fields in order to successfully achieve the SBS process. Notice how

[3] Nomenclature of 'pump' and 'probe' were chosen here for continuity. In the literature, the probe is commonly referred to as the Stokes field.

this field energy density is described by the change in the dielectric constant ($\Delta\epsilon$) due to the increase in the density change of the material ($\Delta\rho$). The electrostriction coefficient is defined as: $\gamma_e = \rho\frac{\partial\epsilon}{\partial\rho}$. Furthermore, this change in energy must obey the first law of thermodynamics, i.e. the work done to compress the material is equal to the change in light field energy density:

$$\Delta W = -\rho_e \frac{\Delta\rho}{\rho} \tag{1.10}$$

Where ρ_e is defined as the electrostriction pressure due to the presence of the electric field: $\rho_e = -\frac{1}{2}\gamma_e\langle\tilde{E}^2\rangle$. Thus, this gives rise to the electric field force which is the source term of the acoustic wave equation:

$$\boldsymbol{F} = -\nabla\rho_e = \frac{1}{2}\gamma_e\nabla\langle\tilde{E}^2\rangle \tag{1.11}$$

$$\nabla\cdot\boldsymbol{F} = -\gamma_e q^2\left[A_{pump}A^*_{probe}e^{i(qz-\Omega t)} + c.c.\right] \tag{1.12}$$

This driving term can now be put into the acoustic wave equation while making two assumptions. The equation can be simplified by neglecting the second order derivatives by considering that the acoustic wave amplitude varies slowly over both space and time. The solution provides:

$$(4\pi^2\nu_B^2 - \Omega^2 - i\Omega\Gamma_B) - 2i\Omega\frac{\partial\rho}{\partial t} - 2iqv_s^2\frac{\partial\rho}{\partial z} = \gamma_e q^2 A_{pump}A^*_{probe} \tag{1.13}$$

Where Γ_B is the Brillouin linewidth defined as: $\Gamma_B = q^2\Gamma'$, who is inversely related to the lifetime of the acoustic phonon. Since these acoustic phonons generated here are strongly damped, the propagation distance is very short before being absorbed, thus the spatial derivative can be ignored and assuming steady-state drops the time derivative:

$$\rho(z,t) = \frac{\gamma_e q^2 A_{pump} A^*_{probe}}{4\pi^2 \nu_B^2 - \Omega^2 - i\Omega\Gamma_B} \tag{1.14}$$

This solution describes the coupling between the optical fields and the resultant phonon, but we also need to explore how the optical fields evolve together. We start with the wave equation for the optical waves:

$$\frac{\partial^2 \tilde{E}}{\partial z^2} - \frac{1}{\left(\frac{c}{n}\right)^2}\frac{\partial^2 \tilde{E}}{\partial t^2} = \frac{1}{\epsilon_0 c^2}\frac{\partial^2 \tilde{P}}{\partial t^2} \tag{1.15}$$

This wave equation can be considered for both the pump and probe fields. The driving term of this wave equation is given by the total nonlinear polarization. The total polarization is: $P = P_L + \tilde{P}$ and the nonlinear contribution arises from changes in the nonlinear susceptibility, which can be thought of as a change in the dielectric constant due to the incident light fields by: $\tilde{P} = \epsilon_0 \Delta\chi\tilde{E} = \epsilon_0 \Delta\epsilon\tilde{E} = \frac{\epsilon_0 \gamma_e \tilde{\rho}}{\rho_0}\tilde{E}$. Just as was done with the acoustic wave driving term, we can consider the phase-matched driving terms by:

$$\tilde{P}_{pump} = p_{pump} e^{i(k_{pump} z - 2\pi\nu_{pump} t)} + c.c. \tag{1.16}$$

$$\tilde{P}_{probe} = p_{probe} e^{i(k_{probe} z - 2\pi\nu_{probe} t)} + c.c. \tag{1.17}$$

Where the respective polarization wave amplitudes are:

$$p_{pump} = \frac{\epsilon_0 \gamma_e \rho}{\rho_0} A_{probe} \tag{1.18}$$

$$p_{probe} = \frac{\epsilon_0 \gamma_e \rho^*}{\rho_0} A_{pump} \tag{1.19}$$

Thus, we can return to the wave equation to obtain:

$$\frac{\partial A_{pump}}{\partial z} + \frac{1}{\frac{c}{n}}\frac{\partial A_{pump}}{\partial t} = \frac{i\pi\nu\gamma_e}{nc\rho_0}\rho A_{probe} \tag{1.20}$$

$$-\frac{\partial A_{probe}}{\partial z}+\frac{1}{\frac{c}{n}}\frac{\partial A_{probe}}{\partial t}=\frac{i\pi\nu\gamma_e}{nc\rho_0}\rho^* A_{pump} \tag{1.21}$$

Notice that now we are considering that $\nu_{pump}\approx\nu_{probe}\approx\nu$. Additionally, again considering steady-state conditions we can ignore the time derivatives and we arrive at the field amplitude coupled equations:

$$\frac{\partial A_{pump}}{\partial z}=\frac{i\epsilon_0\pi\nu q^2\gamma_e^2}{nc\rho_0}\frac{\left|A_{probe}\right|^2 A_{pump}}{4\pi^2\nu_B^2-\Omega^2-i\Omega\Gamma_B} \tag{1.22}$$

$$\frac{\partial A_{probe}}{\partial z}=\frac{-i\epsilon_0\pi\nu q^2\gamma_e^2}{nc\rho_0}\frac{\left|A_{pump}\right|^2 A_{probe}}{4\pi^2\nu_B^2-\Omega^2+i\Omega\Gamma_B} \tag{1.23}$$

Using the definition of intensity as: $I=2n\epsilon_0 cAA^*$. We obtain:

$$\frac{dI_{pump}}{dz}=-gI_{pump}I_{probe} \tag{1.24}$$

$$\frac{dI_{probe}}{dz}=-gI_{pump}I_{probe} \tag{1.25}$$

Which leads us to the gain and center-line gain factor equations. The result of this analysis is that the SBS process imparts an exponential growth of the probe beam: $I_{probe}(z)=I_{probe}(L)e^{gI_{pump}(L-z)}$. The purpose of showing this calculation is to highlight the nonlinear nature of SBS and motivate the use of high intensity light fields to generate strong signals.

1.2.2 Stimulated Brillouin scattering

A "stimulated process" is one that, in general, requires the triggering or enhancement by an external stimulus or input; otherwise, the process would occur *spontaneously* without external intervention. Such a distinction can be drawn for our purposes between stimulated Brillouin scattering and spontaneous Brillouin scattering when classifying light scattering

events in a material system. As discussed previously, a light scattering event is the result of fluctuations in the optical properties of a material; the root cause of the aforementioned fluctuations determines the process in which the event occurs. For example, a spontaneous Brillouin scattering event is typically defined as fluctuations in the dielectric constant of the material due to either thermal or quantum-mechanical zero-point effects. Conversely, a stimulated Brillouin scattering event's fluctuations come from the presence of an external light field and manifests as a nonlinear interaction between the pump and Stokes fields via a moving acoustic wave. The nonlinear exponential growth achieved in Stokes wave is what enables SBS to have much higher possible efficiency than its spontaneous counterpart [21].

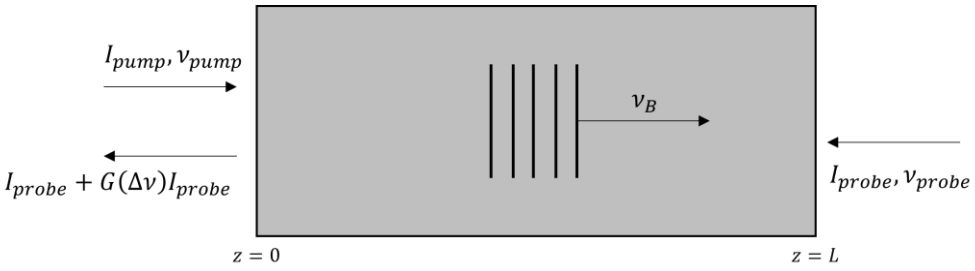

Fig. 1.2. Schematic illustrating the stimulated (Stokes) Brillouin scattering process.

Two counterpropagating fields, pump and probe, beat together and generate a moving acoustic wave through electrostriction[4]. The material undergoes changes in optical properties, namely refractive index, that cause scattering of the pump light. Essentially this creates a moving Bragg grating in the medium at the acoustic velocity (ν_s). The scattered light's frequency is subsequently downshifted due to the Doppler shift of the traveling

[4] SBS can also be the result of absorption; however, this occurs much less commonly and for the purposes of this thesis will be ignored.

acoustic phonon. By design, the resultant frequency now matches that of the probe beam and will combine to generate more acoustic phonons which in turn generate more scattering and so on and so forth. For our purposes, when we are operating in an SBS amplifier configuration, the frequency difference between the external light beams is known *a priori* and is tuned to efficiently drive the coupling between acoustic and optical waves.

$$\Delta\nu = \left|\nu_{pump} - \nu_{probe}\right| \tag{1.26}$$

As the frequency difference between the pump (ν_{pump}) and probe (ν_{probe}) is tuned near the phonon frequency, the scattered light acquires a Lorentzian distribution of frequency centered at ν_B with a linewidth of Γ_B. Where these quantities can be described as the following:

$$\Omega = \nu_B = \frac{2n}{c} v_s \nu \sin\left(\frac{\theta}{2}\right) \tag{1.27}$$

$$2\pi\Gamma_B = 4\pi^2 \left(\frac{2n}{c}\nu\right) \Gamma' \tag{1.28}$$

Where n is the refractive index, ν_s is the speed of sound, c is the speed of light, ν is the photon frequency, θ is the scattering angle, and Γ' is the damping parameter. The linewidth of the gain spectrum is related to the lifetime of the acoustic wave ($\tau_p = \Gamma_B^{-1}$). Experimentally, we can ascertain the SBS signal from the gain observed in the transmitted probe beam. Following from Eqns. 1.22-1.25:

$$\mathrm{G}(\Delta\nu) = \frac{\Delta I_{probe}(\Delta\nu)}{I_{probe}} = g(\Delta\nu) I_{pump} L \tag{1.29a}$$

$$\mathrm{g}(\Delta\nu) = \mathrm{g}_0 \frac{(\Gamma_B/2)^2}{(\Delta\nu - \nu_B)^2 + (\Gamma_B/2)^2} \tag{1.29b}$$

$$\mathrm{g}_0 = \frac{4\pi\gamma_e^2 \nu^3}{c^4 \rho \nu_B \Gamma_B} \tag{1.29c}$$

The gain in the transmitted probe beam is related to the intensity of the pump (I_{pump}), L the interaction length, and the Lorentzian shaped gain factor. The peak value of the Brillouin gain factor occurs at ν_B and is also known as the line-center gain factor (g_0) which depends on a number of material properties such as the electrostrictive constant (γ_e) and the mass density (ρ).

SBS was first observed in 1964 [23] and since then has been used in several kinds of applications. For example, the Brillouin gain from the nonlinear SBS process can be used as a laser when placed in a cavity [24] and can also amplify small signals [25,26]. SBS, specifically used in fibers, can be fashioned into distributed fiber sensors which can sense temperature and strain changes [27,28] as they both affect the refractive index of the fiber. Recently, which will be discussed in the following section, SBS has been introduced towards biomedical applications as a competitive approach to spontaneous Brillouin based microscopy, a well-established technique in biomechanical measurements.

1.2.3 Continuous wave stimulated Brillouin scattering microscopy

As spontaneous Brillouin scattering has begun to exhaust its avenues for speed improvements, stimulated Brillouin offers a new horizon for researchers to explore. The exploitation of SBS in microscopy applications began with continuous wave (CW) lasers, for both pump and probe beams. As with the differing natures of the two scattering phenomena described above, SBS differs from spontaneous in that it needs to implement two beams of light rather than just one: one with a fixed frequency and one that can be

tuned on the order of GHz. These two beams can originate from the same laser source but often in CW SBS they are two separate lasers, see Fig. 1.3. In CW SBS, this frequency difference is controlled, typically, by a voltage source that sweeps an internal grating in one of the lasers via a piezo to rapidly change (roughly hundreds of GHz/s) the relative frequency difference between the two beams. Monitoring this GHz frequency difference requires the combination of a high-speed photodetector and a signal analyzer with ample bandwidth. For biological measurements, more often than not, a 2GHz scan range is appropriate as most biological samples have Brillouin shifts around 5GHz thus a scan between 4GHz and 6GHz is enough to capture the spectra. Wider scan ranges can be done but are not typical considering that most Brillouin linewidths of biological materials are on the order of hundreds of MHz[5] as well as increasing scan range will increase the time it takes to complete a frequency scan.

[5] The linewidth of water at 780nm is ~300MHz.

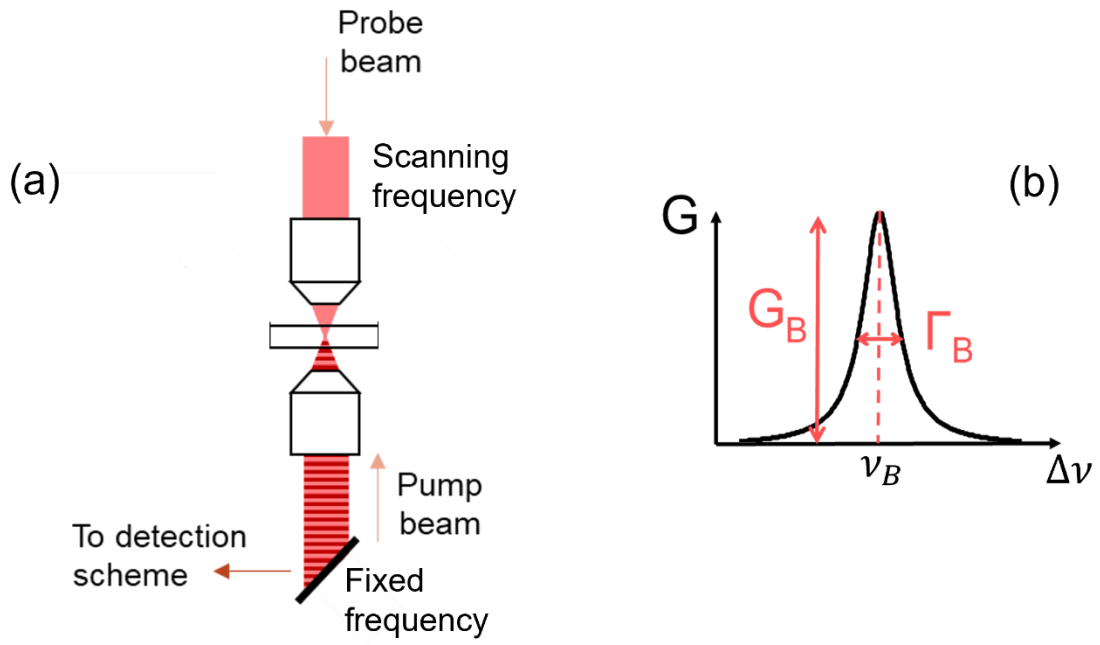

Fig. 1.3. (a) Simplified schematic of CW SBS microscope with counterpropagating beams. (b) Example of resultant stimulated Brillouin gain spectrum.

It is important for achieving optimal gain measurements to have good alignment of the focusing region between the two microscope objectives. This is referred to as crossing efficiency (η) [29]. This term is introduced with respect to SBS microscopy because in optical fibers there is complete overlap of the beams and as such this drawback is not a concern. Notwithstanding, careful alignment of the counterpropagating beams is crucial to achieving optimal overlap without reducing gain significantly. Low numerical aperture (NA) objectives are used in order to have interaction lengths on the order of tens of microns. We can rewrite Eq. 1.29(a) to incorporate this factor as well as account of the interaction region becoming the focusing region between the two microscopes as [30]:

$$\mathrm{G}(\Delta\nu) = g(\Delta\nu) I_{pump} L = \eta g(\Delta\nu) P_{pump} \frac{2}{\lambda} \tag{1.30}$$

Where P_{pump} is the pump beam peak power and λ is the probe laser wavelength. This expression assumes constant power over the interaction length, i.e. no attenuation. As a result of these small interaction lengths and taking photodamage damage of biological samples into consideration, which will be discussed in greater detail in the following chapter, SBS microscopy exists in the 'low-gain' regime. The low-gain regime is defined as small signal gains of $\sim 10^{-5} - 10^{-3}$. In biological SBS measurements, the limiting factors with respect to gain are consequently the interaction lengths and power constraints.

One more obvious distinction between spontaneous and stimulated Brillouin microscopy I would like to call attention to is the detection methodology. It is common in spontaneous Brillouin spectroscopy to use electron-multiplying charged-coupled devices (EMCCDs) used to image the spectra due to the high dynamic range requirements and low photon numbers collected. This is in stark contrast to what is seen in CW SBS detection where the Brillouin spectra has to be collected *in addition* to very high background probe light levels. To put it in perspective, CW SBS microscopy achieves gain ($\sim 10^{-5}$) of the transmitted probe beam thus a majority of the light incident on the, typically used, photodiode detectors is from background probe light. To combat this, CW SBS detection customarily includes lock-in amplifiers in order to sensitively detect the probe gain [31]. This architecture entails intensity modulation of the pump beam in which the Brillouin-interacted transmitted probe beam acquires whereas the background light does not. For example, this can be done by sending the pump beam through an acousto-optic modulator (AOM) driven with a 1MHz sine wave. The lock-in amplified then uses a reference 1MHz

sine wave and the AC signal from the photodetector to demodulate and extract the Brillouin gain from the background light. Recent demonstrations of CW SBS microscopy based on this technology have been somewhat successful in reducing acquisition times compared to spontaneous Brillouin microscopy and have shown this in liquids (~2-5ms acquisition times) [30,32,33] and C. elegans (~20ms acquisition times) [34]. While making modest speed ups possible, there is still much room for improvement to fully utilize the nonlinear nature of the SBS process.

1.2.4 Pulsed stimulated Brillouin scattering microscopy

As it stands, to improve the spectral acquisition time of SBS microscopes, the SNRs must be improved upon. Throughout this thesis we will see how these two quantities are explicitly tied to one another as accessing higher SNR means that you can 'pay' for faster spectral measurements with that improved signal. This of course assumes that the system has the technical capabilities to experimentally reach those speeds, but this will be explored in greater detail below.

The most obvious way to improve SNR is to leverage higher intensity light beams. In the context of SBS microscopy, this means moving from CW lasers to pulsed lasers. For decades, pulsed lasers have been used in SBS spectroscopy in other application spaces such as fiber-optic telecommunication and fiber sensing. Technologies in this space utilize nanosecond pulses in fiber-optic distributed sensing for temperature or strain measurements [35–37], but also can be found in optical signal processing [38] and on-chip

waveguides [39]. Of course, using picosecond or femtosecond pulses would be more intense than nanosecond pulses, but when considering the lifetime of the acoustic waves present in the SBS process, nanosecond pulses end up offering the highest intensity while still capturing the effect efficiently. One of the reasons why pulsed laser sources have yet to become the standard in SBS microscopy is that nanosecond pulsed lasers with adequate parameters for Brillouin microscopy in the visible regime, to date, do not exist commercially. SBS microscopy is done in the visible wavelength regime due to the wavelength dependence of the gain signal ($\propto \frac{1}{\lambda^4}$), thus it is prudent to operate at the lowest possible wavelength; however, the absorption of water ought to be taken into consideration as well which is why SBS microscopy typically is done at 780nm. Furthermore, the application space of microscopy has small interaction lengths compared to fiber-optic applications and biological samples place stringent power limitations that together relegate SBS measurements of biological samples to the 'low-gain' regime. The 'low-gain' regime exists where the possible gain of the interaction is as low as $10^{-4} - 10^{-5}$ meaning that the Brillouin amplified signal is only a small fraction of the detected signal, thus leading to low SNR. It is also important to point out that as long as appropriate pulse durations are chosen, i.e. that it is long enough to maintain a transform limited bandwidth narrower than the Brillouin linewidth of the sample, that it does not become a limiting factor in Brillouin gain reduction. This leaves a clear gap in the field where optimal source parameters are yet to be explored.

In addition to source-side optimization needs, the detection parameters of SBS are severely understudied. As will be outlined in a later chapter, SBS microscopy has long

suffered from the use of nonoptimal detection, where an inefficient power balance between the pump and probe beams is used to avoid saturating the photodetector. In light of this, two recent attempts to implement pulsed lasers into SBS microscopy [40,41] have failed to deliver virtually any spectral acquisition speed improvements compared to CW SBS microscopy despite the potential benefits possible. Additionally, dual balanced detection was used for these setups as it reduces relative intensity noise (RIN) in the measured probe beam; however, this comes at the cost of doubling the shot noise. As such, it is important to choose what method of detection (lock-in detection, balanced detection, direct detection, etc.) is needed based on the limiting noise sources. Chapter 3 will explore this concept further as we performed a detailed noise analysis before choosing our detection methodology.

Chapter 2: Stimulated Brillouin scattering flow cytometry[6]

2.1 Measuring cell biomechanics

Cells are complex machines that sense and respond to their environmental cues, thus making their biomechanical behavior an important process to study. The mechanical interactions they experience can alter cellular functions, i.e. migration tendencies [42,43], cell proliferation [44], and gene expression [45], as well as effecting morphogenesis [46] and metastasis [47]. Notwithstanding, there have been numerous methods developed to extract biomechanical markers, specifically elastic modulus, on the cellular level: atomic force microscopy (AFM) [48], micropipette aspiration [49], microrheology [50], and deformable microbeads [51] to name a few. While they have uncovered a plethora of information and have gained great interest in the field, all these instruments either require contact, are significantly invasive, or only gather global mechanical information from the samples.

Evidently this unveils an interesting relationship that has recently been realized [52]: that there is a clear trade-off between how much mechanical information can be ascertained using a given modality and its respective measurement throughput. To give a specific example, cell deformability based methods, which only access whole cell

[6] Chapter adapted from a peer-reviewed journal article: J. R. Rosvold, G. Zanini, C. Handler, E. Frank, J. Li, M. Vitolo, S. Martin, and G. Scarcelli. "Stimulated Brillouin scattering flow cytometry." Biomedical Optics Express (submitted).

mechanical signatures, have begun to be integrated with flow cytometry [53–55] thus achieving measurements of >1000 cells per experiment, but critically lack the resolution to illustrate subcellular structures like the cell nucleus. Ideally, a system would exist with subcellular resolutions to analyze vast biomechanical information while also having high measurement throughput. To address this gap in the field, spontaneous Brillouin scattering was proposed in combination with a flow cytometry scheme [14,56], but lacked the spectral acquisition speeds to truly be considered 'high throughput' as it could only measure ~200 cells per hour. As such, there is a need to speed up spectral acquisitions to make Brillouin microscopy more suitable for high throughput measurements of large-scale mechanical phenotyping and to fill the gap in the field of biomechanical analysis, breaking free of the tradeoff between measurement throughput and mechanical information content current instruments suffer from.

2.2 Experimental methods

2.2.1 Experimental configuration and acquisition

As an example, to illustrate how Brillouin microscopy can be used to investigate the mechanical properties of suspended cells in flow, we built a high-speed Brillouin flow cytometer, see Fig. 2.1(a), based on our state-of-the-art CW SBS microscope [33]. In this case, a 1MHz amplitude modulated CW pump laser (ν_{pump}) illuminates the sample from below while a counterpropagating CW probe (ν_{probe}) is focused from above. Using the known frequency difference between the pump and probe, we can extract the peak position

through Lorentzian least-square fitting of the measured spectra. The acquisition time of each measured spectra is 5ms. Fig 2.1(b) is a widefield image of our flow cytometry measurements in a 50μm × 50μm straight PMMA microfluidic channel (microfluidic ChipShop, GmbH). The size of the channel was chosen to be large enough for cells to pass through while also not being too large in that many cells would miss the Brillouin interaction region at the center of the channel. A syringe pump is connected to the channel and controls the flow rate of the cells suspended in a 10% OptiPrep medium. We experimentally determined that this concentration of density gradient medium resulted in the best conditions for flow with albeit moderate clumping of cells in flow. As the cells flow through the channel, we take continuous Brillouin spectra measurements. When a cell passes through the interaction region of the pump and probe beams, we collect the Brillouin signal of the cell. Fig 2.1(c) shows the distribution of the number of points collected per cell where the cell diameter is roughly 20μm. On average, we obtain ~4-5 points per cell which is dependent on a number of factors namely: the cells size, the position of the cell in the channel, and the relative speed of the cell. It should be noted that using a sheath flow configuration would result in less spread in the distribution of points per cell as a larger number of cells would flow through the center of the channel and consequently the focus of the counterpropagating laser beams. However, a previous demonstration of spontaneous Brillouin flow cytometry validated that obtaining ~4-5 points per cell was sufficient to recapitulate the cell population in flow compared with 2D Brillouin images [56]. In Figs. 2.1(d) and 2.1(e), an experimental example of the acquired water and cell spectra are shown

respectively. The frequency shift is determined via Lorentzian least-square fitting of the data.

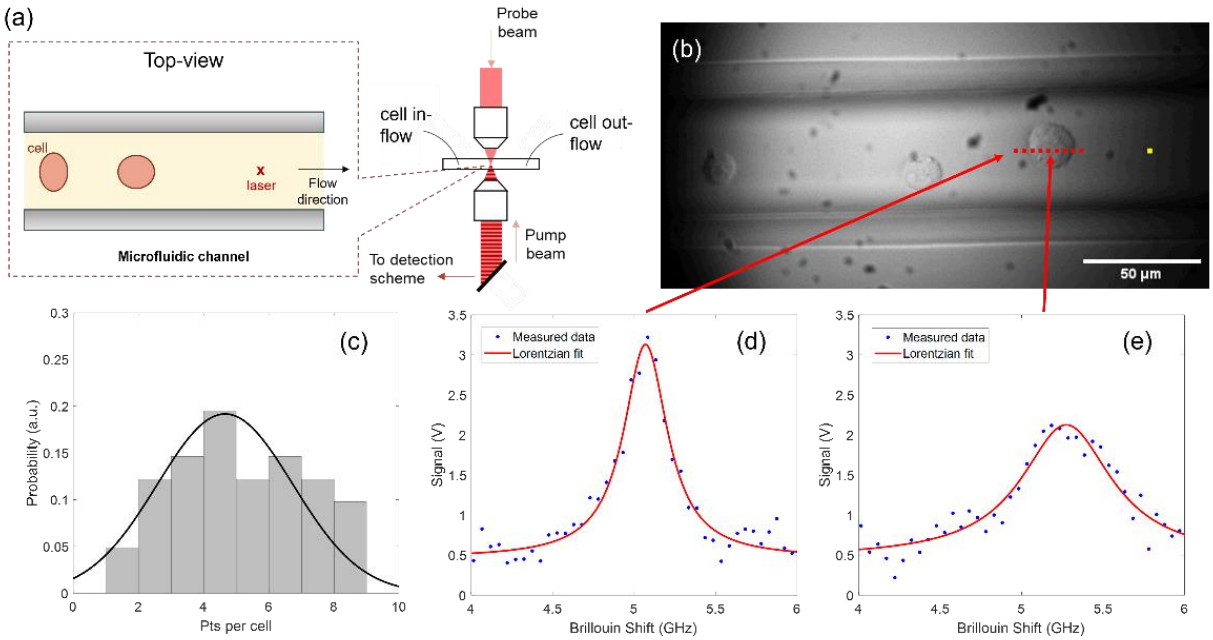

Fig. 2.1. (a) Simplified schematic of the SBS flow cytometer. The inset sketch shows a magnified top-view of the microfluidic channel. (b) Widefield image of cells flowing through the microfluidic channel. Yellow dot represents the laser interaction region with red dots representing example sampling points. (c) Distribution of the number of sampled points per cell over a typical experiment. Experimentally attained Brillouin spectra of (d) medium and (e) the cell at experimental conditions.

2.2.2 Experimental setup

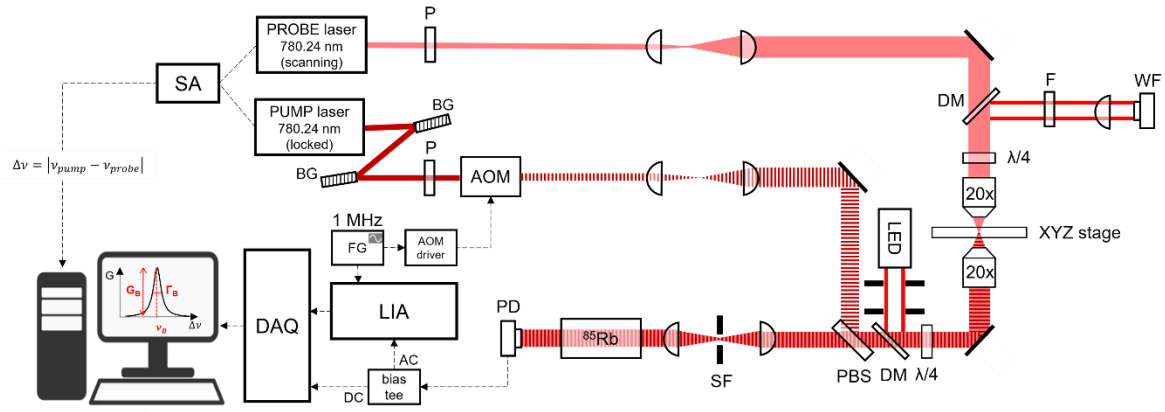

Fig. 2.2. Simplified diagram of CW SBS spectrometer. P: polarizer, λ/4: quarter-wave plate, DM: dichroic mirror, PBS: polarizing beam splitter, SF: spatial filter, PD: photodetector, AOM: acousto-optic modulator, DAQ: data acquisition card, SA: signal analyzer, BG: bragg grating, FG: function generator, LIA: lock-in amplifier, LED: light emitting diode.

Our CW SBS spectrometer (see Fig. 2.2) uses two CW single-frequency, tunable lasers at 780nm with low-noise (~100kHz linewidth) that feed the probe (Toptica DL pro) and pump (Toptica TA pro) arms. Along the pump path, the frequency is locked to an ^{85}Rb absorption line using a vapor-based locking module paired with two Bragg gratings (Optigrate BP-780) that reject (~15dB) extraneous noise. Then the pump is intensity modulated using an acousto-optic modulator (AOM, AOMO 3080-125, Crystal Technologies) at 1MHz. The AOM is driven by a function generator that also provides the lock-in amplifier (LIA, Zurich Instruments UHF) with a reference signal used for demodulation of the detected signal. Meanwhile, on the probe path, the beam is constantly being scanned around the acoustic wave resonance by sweeping the piezo voltage of the

laser and is ultimately the transmitted beam that is detected by the amplified photodetector (Thorlabs PDA36A2). Once detected, the signal is split with a bias tee (MiniCircuits ZFBT-4R2GW+) into DC and AC signals. The DC is used to monitor the baseline probe signal level whereas the AC is sent to the LIA, who is referenced by the pump modulation frequency, to extract the amplified Brillouin signal from the high probe background level. Background modulated pump stray light is reduced by using the combination of a spatial filter and a hot ^{85}Rb vapor cell (Precision Glassblowing) before the photodetector. The beam frequency between the pump and probe beams is monitored by a signal analyzer (Keysight N9000B) which provides the frequency axis component of the extracted SBS spectra.

2.3 Flow cytometer characterization

2.3.1 Stimulated Brillouin scattering system performance

Figures 2.3(a) and 2.3(b) show the shot noise limited operation of our system down to 5ms acquisition time taken at experimental conditions of 150mW of pump average power and 18mW of probe average power. To acquire the Brillouin spectra, the probe frequency is scanned (at 400 GHz/s) over a 2GHz range (from ~4GHz to ~6GHz) for experiments of water and cells. For proper Nyquist sampling, the read rate of the DAQ was set to be greater than twice the bandwidth of the lock-in amplifier. For the data shown below, 100 samples of water spectra were acquired in a 50μm × 50μm straight microfluidic channel, and each spectrum was fit with a Lorentzian to estimate the Brillouin shift and linewidth. The

frequency precision (δ_{ν_B}) is then defined as the standard deviation of the Brillouin shift estimates over the 100 spectra acquired. As expected, our frequency precision measurements follow a Gaussian distribution as seen in Fig. 2.3(b). We achieve ~7.5MHz precision at our experimental conditions which is known to give high-quality Brillouin measurements for cells. At our shortest exposure condition, 5ms, we are capable of ~7.5MHz precision meaning we could theoretically run shorter exposure while still maintaining the 10MHz precision limit; however, our system is technically limited by the scanning mechanisms of the probe laser, i.e. the piezo inside the probe laser module. To reach the ultimate scanning speed, an external scanning module would have to be used; either an acousto-optic modulator (AOM) or an electro-optic modulator (EOM).

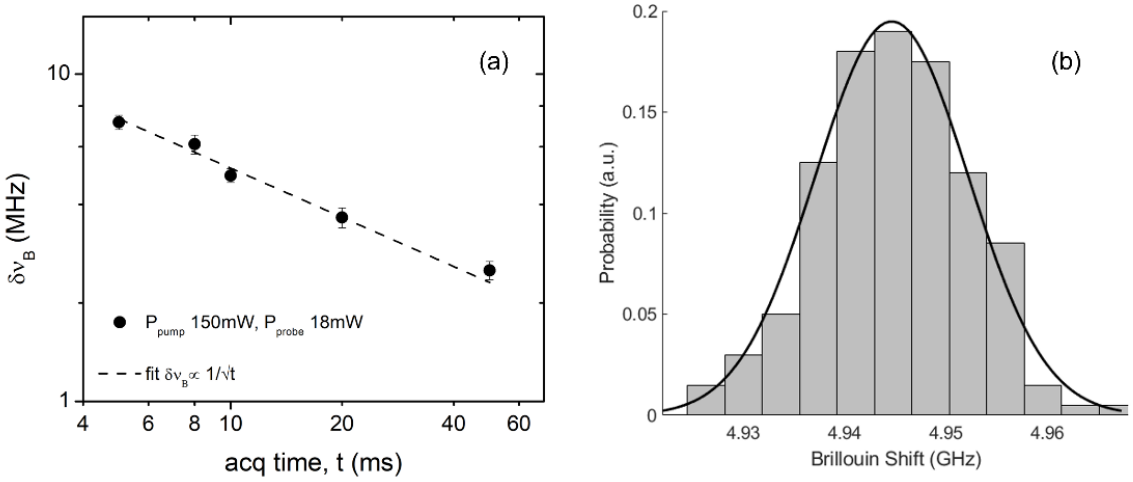

Fig. 2.3. Experimental data of water to demonstrate system performance. (a) Shift precision (δ_{ν_B}) for 100 spectra of water in the 50μm × 50μm straight microfluidic channel with typical measurement conditions while varying acquisition time. Pump and probe average powers were held constant at 150mW and 18mW respectively. Dashed line represents linear fit of the data.

Error bars are the standard deviation over the 100 acquisitions. (b) Distribution of the 100 Brillouin shifts fit with a Gaussian.

2.3.2 Throughput capability

To estimate our SBS flow cytometer speed capabilities we consider a representative measurement segment (~10s in length) as shown in Fig. 2.4. This measurement segment is one of many taken over the course of a measurement trial and contains the Lorentzian-fit Brillouin shifts recorded in a small time window as cells flow through the Brillouin interaction region in the microfluidic channel. As our home-built LabView program is continuously acquiring the Brillouin signal, the measurement segments collect signatures from both the medium and cells which are later analyzed by our post-processing procedure. Figure 2.4 demonstrates that, at our experimental conditions of 5ms spectral time with the measurement segment window of ~10s, we are capable of collecting the information of the 3 unique cells. Between 0-2 s in the window there are no cells passing through the interaction region therefore we can extrapolate from experimental data that our SBS flow cytometer throughput is 3 cells per 8s or 0.375 cells per second. This corresponds to >1,000 cells per hour which is comparable to other high throughput mechanical analyses [52,54,57] while also providing substantially higher mechanical information. As such, this technology would greatly reduce the time required to complete mechanical analysis of large numbers of cells.

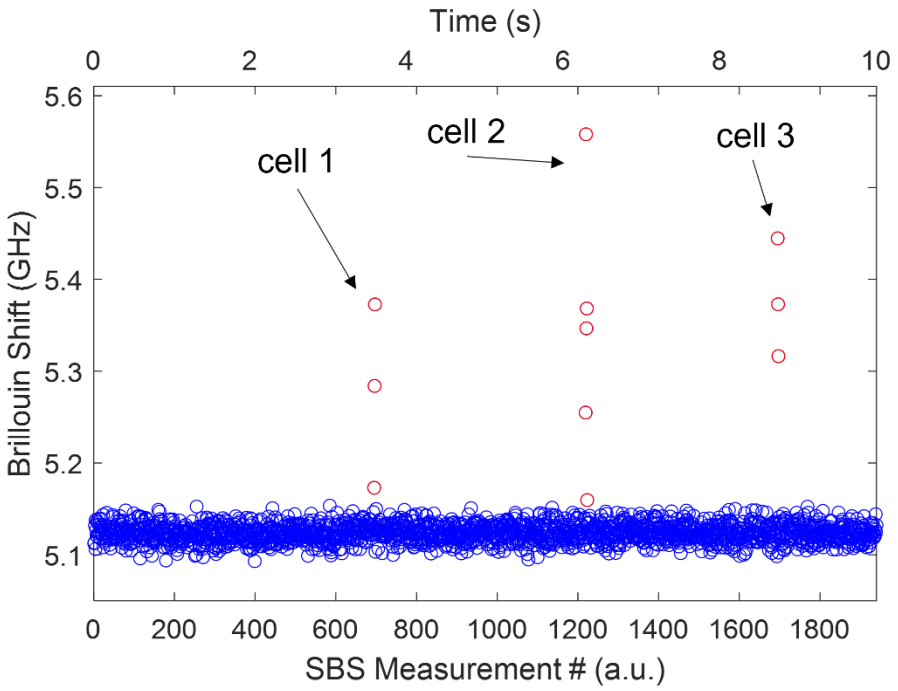

Fig. 2.4. Demonstration of individual measurement segment. Segment of continuously acquired Brillouin shift data as 3 cells flow across the Brillouin interaction region. Total time of measurement segment is ~10s. Circles represent individual 5ms spectral measurements where blue circles are measurements of medium and red circles are measurements of the cells. Arrows indicate different cells.

It should be noted that theoretically our throughput could be much higher given our measurement rate of 200Hz. Our flow cytometer is mainly limited by nonoptimal flow conditions. For example, the clumping of cells reduces the cell flow rate over the course of the measurement trial and employing sheath flow and hydrodynamic focusing [58–61] or droplet microfluidics [62–65] could greatly increase the number of cells passing through the Brillouin interaction region. Assuming adequate control of the relative spacing between consecutive cells, ~5pts per cell and 5pts between the next subsequent

cell, an SBS flow cytometer with our measurement time could reach an overall throughput of ~20 cells per second.

2.4 Cell measurements

2.4.1 Sample preparation

MCF10A M1 cells were gifted by Michele Vitolo and cultured with DMEM/F-12 (Gibco #11330033), 5% Horse Serum (Gibco #16050122), EGF (Peprotech #AF-100-15), Hydrocortisone (Sigma #H-0888), Cholera Toxin (Sigma #C-8052), Insulin (Sigma #I-1882), and Pen/Strep (Gibco #15070063). MDA-MB-231 were acquired from ATCC (ATCC #HTB-26) and cultured with DMEM (ATCC #30-2002), 10% FBS (ATCC #30-2020), and Pen/Strep (Gibco #15070063). Cells were prepared for flow experiments by resuspension in DPBS (Gibco #14190144) or 10% OptiPrep (Sigma #C974P05).

2.4.2 Post-processing of flow data

As described previously, we used a 50μm × 50μm microfluidic channel with a syringe pump to flow cells and collect their Brillouin signal. Once the prepared cells in suspension are loaded into the syringe, we collect measurements of the cells in flow over the course of a ~45min measurement trial. With our home-built LabView acquisition program, we acquire many smaller segments (~10s) of data which are comprised of individual spectral measurements (~2000 × 5ms). During these segments, cells flow across the Brillouin interaction region and are sampled at multiple points by our spectrometer. In post-

processing, our home-built MATLAB script uses a single peak Lorentzian least-square fit of each individual spectral measurement and collects the respective Brillouin information. This collection of spectral information can then be represented as a histogram, see Fig. 2.5(a), which, due to our continuous acquisition, contains data from both the medium used in flow and the cells. We remove the medium signature by fitting a Gaussian to measurements of only the medium and subtracting it from the overall distribution, see Fig. 2.5(b). Once removed, we are left with the cell signature which is composed of both the cytoplasm and nucleus as is shown in Fig. 2.5(c). We can distinguish the two by fitting the cell signature with a linear combination of two Gaussians where the lower Brillouin shift peak position corresponds to the cytoplasm, which is known to be less stiff than the nucleus, and the higher Brillouin shift peak position is the nucleus. Similar post-processing methodology has been demonstrated before and has combined spontaneous Brillouin with fluorescent imaging to confirm that cell nuclei tend to have higher Brillouin shifts when compared to the cytoplasm [56].

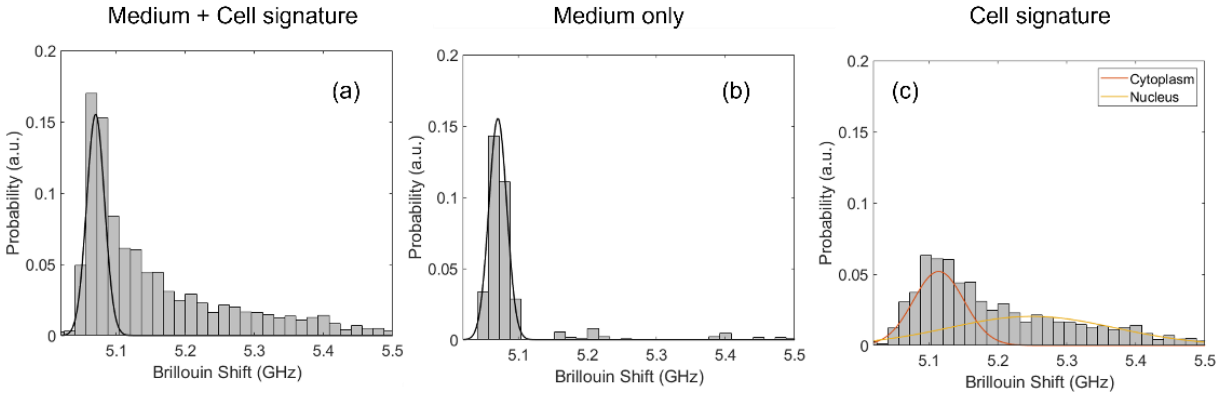

Fig. 2.5. Histograms represent flow experiment data post-processing. (a) Experimental data with Brillouin shift signatures from both the medium and the cells. (b) Experimental data of Brillouin shift of only the medium. Black line represents Gaussian fit to be subtracted from

overall measurement. (c) Extracted cell signature with medium removed. Orange and yellow lines are each Gaussian fits of the cytoplasm and nucleus respectively.

2.4.2 Brillouin shift analysis

During each experiment, our CW SBS flow cytometer sampled hundreds of cells each sampled at multiple points. With our post-processing, described in the previous section, we construct representative cell signature distributions which allow us to understand the mechanical properties of the cell lines at high throughput and compare them. We analyze the Brillouin shift of the nucleus and cytoplasm of each of the two cell lines. In this manner, we are capable of classifying cell populations based on their mechanical signatures.

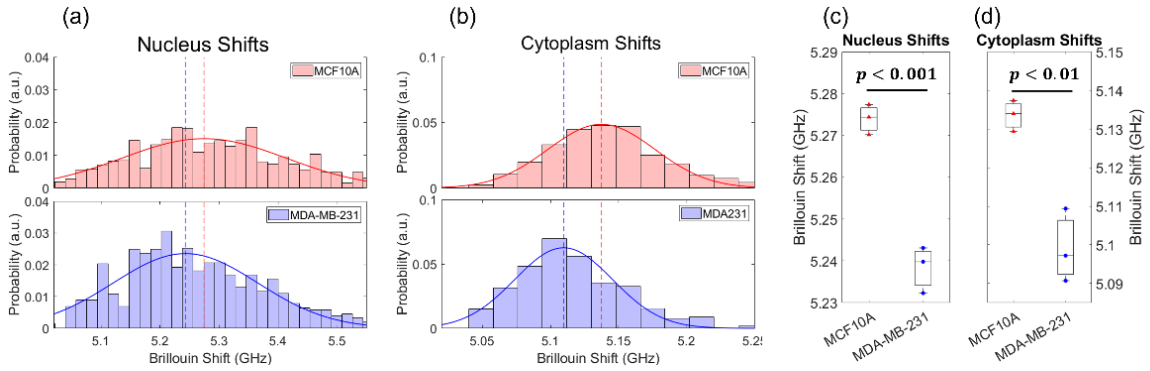

Fig. 2.6. Brillouin shift cell signature results. Representative experiments of MCF10A (top, 280 cells) and MDA-MB-231 (bottom, 311 cells) separated into (a) nucleus signatures and (b) cytoplasm signatures. The red lines depict the Gaussian fits of the MCF10A distributions, and the blue lines show the Gaussian fits of the MDA-MB-231 distributions. The dashed lines in each plot show the central peak location of each fit. (c) and (d) show the Brillouin shift population central peak location for the nucleus and cytoplasm respectively. Three separate experiment runs

for both cell lines were conducted. Statistical significance between the two cell lines was analyzed using a two-sample t-test.

In order to confirm our prediction that MCF10A will have a higher Brillouin shift than MDA-MB-231, we can analyze the Brillouin shifts of the cell lines using our population distributions of three separate experiments for each cell line. As previously mentioned, the cell signatures can be broken down into nucleus and cytoplasm contributions. A representative experiment of MCF10A, shown in Fig. 2.6(a) and 2.6(b) in red, captures the overall mechanics of the population having higher Brillouin shift and thus higher stiffness compared to MDA-MB-231, shown in Fig. 2.6(a) and 2.6(b) in blue. The nucleus shift central peak location of MCF10A for this experiment is at 5.27 GHz while MDA-MB-231 is at 5.24 GHz. The cytoplasm shift central peak location of MCF10A is 5.14 GHz and MDA-MB-231 is 5.11 GHz. We performed a two-sample t-test to confirm the statistical significance between the two cell line nucleus shifts, Fig. 2.6(c), as well as the cytoplasm shifts, Fig. 2.6(d). In both cases of nucleus and cytoplasm, we observe significantly higher Brillouin shifts in MCF10A than MDA-MB-231 in flow.

These findings are consistent with gold-standard mechanical analyses of metastatic potential [57,66–70] and provide validation of our flow cytometer. The resultant lower Brillouin shift, and subsequently softer, signature seen in the metastatic MDA-MB-231 when compared to MCF10A can be largely attributed to cytoskeleton alterations and thus is linked to a characteristic reduction in adhesion [71] and higher invasiveness [72] of cancer cells. One of the main benefits of using Brillouin for these measurements is the

fidelity it provides with respect to being all-optical and thus not perturbing the cell such as other current technologies, thus alleviating any artifacts due that cells are prone to through mechanical stimulation.

2.4.2 Brillouin linewidth analysis

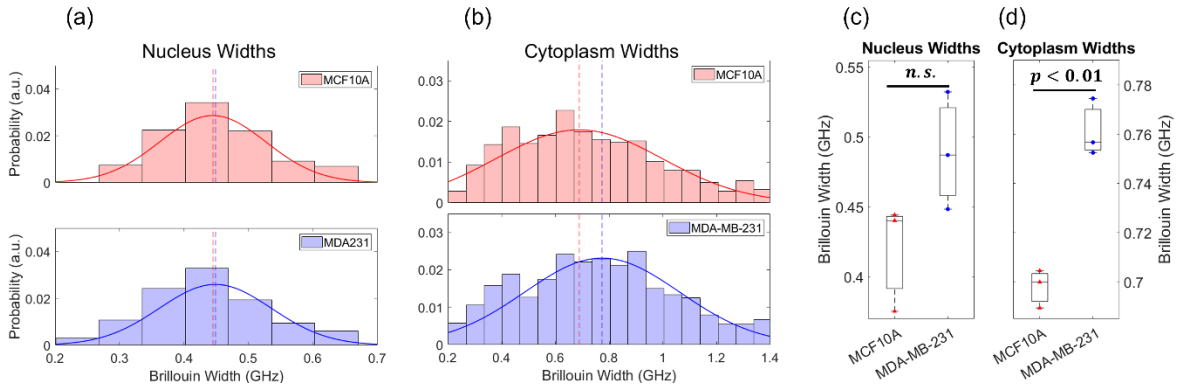

Fig. 2.7. Brillouin linewidth cell signature results. Representative experiments of MCF10A (top, 373 cells) and MDA-MB-231 (bottom, 311 cells) separated into (a) nucleus signatures and (b) cytoplasm signatures. The red lines depict the Gaussian fits of the MCF10A distributions, and the blue lines show the Gaussian fits of the MDA-MB-231 distributions. The dashed lines in each plot show the central peak location of each fit. (c) and (d) show the Brillouin linewidth population central peak location for nucleus and cytoplasm respectively. Three separate experiment runs for both cell lines were conducted. Statistical significance between the two cell lines was analyzed using a two-sample t-test.

In addition to measuring the Brillouin shift of the cells in flow, this architecture is capable of extracting the Brillouin linewidth since the system is not based on spectral dispersive elements (~500MHz resolution) but rather on laser interactions (~100kHz

resolution). One of the main benefits of using SBS is that the spectrometer linewidth is limited only by the inherent laser linewidth which is orders of magnitude smaller than the Brillouin spectrum linewidth, thus our analysis can include information that spontaneous Brillouin systems are not as sensitive to due to the spectrometer point spread function (PSF). Figure 2.7 shows our MCF10A and MDA-MB-231 population analysis for Brillouin linewidth. Since the Brillouin linewidth is inversely proportional to the lifetime of the generated acoustic waves, the linewidth is related to imaginary part of the complex longitudinal modulus: $\Gamma_B \propto M''$, linewidth is a proxy measure of viscosity. A representative experiment is shown in Fig. 2.7(a) and 2.7(b). We observe similar linewidth results for both the nucleus central peak location of MCF10A at 444 MHz and MDA-MB-231 at 449 MHz; however, the cytoplasm distribution has a different behavior with MCF10A at 689 MHz and MDA-MB-231 at 775 MHz respectively. We performed a two-sample t-test to confirm the statistical significance between the two cell line nucleus linewidths, Fig. 2.7(c), as well as the cytoplasm linewidths, Fig. 2.7(d). Our analysis suggests that MDA-MB-231, the metastatic cell line, has a more viscous cytoplasm than the normal MCF10A cell line while the nucleus linewidths between the two cell lines were not significantly different. From literature it has been reported that MDA-MB-231 displays lowered viscosity compared to MCF10A [73] using magnetic rotational spectroscopy at low frequencies. However, these experiments were performed in attached cells which may exhibit different mechanical properties than cells under suspended conditions.

2.5 Conclusion

In this work, we presented the combination of state-of-the-art CW SBS with flow cytometry to achieve higher throughput mechanical measurements of cells. We analyzed the Brillouin shift signatures of both the nucleus and cytoplasm of MCF10A and MDA-MB-231. This analysis between populations allows researchers to identify biomechanical differences and to probe their connection with how the cells function and how they behave. Our CW SBS flow cytometry setup is capable of measuring continuously at a rate of 200Hz, given by the 5ms spectral acquisition speeds which marks a 10x improvement in measurement time compared to a previous implementation of spontaneous Brillouin flow cytometry [56]. This resulted in an overall throughput of 0.375 cells per second. Our throughput is limited by nonoptimal flow conditions and clumping of cells, which in turn slows down the flow rates and frequency of cells passing through the interaction region. Further improvements to a setup such as this one could utilize advanced microfluidic techniques to fully exploit the speedup potential that CW SBS systems offer. The theoretical throughput of a system leveraging microfluidic techniques such as these could exceed ~20 cells per second.

Chapter 3: Design and proof-of-principle validation of an optimal source/detection scheme of stimulated Brillouin scattering spectroscopy[7]

3.1 Optimal power balance for high signal-to-noise ratio Brillouin measurements

In SBS spectroscopy, it is desirable to increase the pump and probe power in order to increase the Brillouin gain and achieve higher SNR measurements; however, in applications such as microscopy, the sample introduces limits on the average power and peak powers due to photodamage constraints. Pulsing the pump and probe can improve the SNR for a fixed average power [40,41], but the minimum duty cycle is constrained by the peak power photodamage threshold, limiting the SNR improvement. Furthermore, the balance of power between the pump and probe beams should be considered for optimal SNR [40]. When operating in shot-noise conditions, the SNR has the following dependence on the pump and probe powers: $SNR \propto P_{pump}^2 P_{probe}$ [33] where the SNR is defined as the change in the measured probe signal voltage squared due to Brillouin amplification divided by the shot-noise limited uncertainty in the measured probe signal power. Although SNR is maximized for a peak power ratio of $P_{pump}: P_{probe} = 2:1$, it is not a trivial matter to use this optimal power balance, since detector saturation prohibits the use of high probe power. Most commercial high-speed detectors saturate between 1-20mW. There are a number of parameters that can affect the saturation limit for photodetectors, such as the reverse bias

[7] Chapter adapted from a peer-reviewed journal article: J. R. Rosvold, J. Murray, G. Zanini, B. Redding, and G. Scarcelli. "Impact of polarization pulling on optimal spectrometer design for stimulated Brillouin scattering microscopy." APL Photonics (in-review).

voltage used, detector size, load resistance, etc., but even operating at optimal conditions leads to, at best, saturation powers of tens of milliwatts. Even using large area detectors, while promising, can help increase the saturation power of the detector due to their increased noise equivalent power (NEP) and thus responsivity, but does have downsides when it comes to noise and response times. As such, detectors with saturation powers beyond 20mW are not commercially available. For example, this limitation results in the following: assuming an average power of 200 mW and a duty cycle of 10%, allocating 33% of the power to the probe would lead to a peak probe power of 667 mW—well beyond the saturation threshold of high-speed photodetectors. Instead, to avoid saturating a detector with a saturation power of 20 mW (as used in Refs. [33,34,40]) only 1% of the power can be allocated to the probe beam, resulting in 75% reduction in SNR compared to the optimal ratio. Ultimately, these constraints on SBS measurements result in acquisition times that approach those used in spontaneous Brillouin schemes with little or no improvement.

However, a polarization pulling scheme can help circumvent these limitations by discarding much of the probe power. This approach has still resulted in the same SNR scaling ($SNR \propto P_{pump}^2 P_{probe}$) but the detected power can be greatly reduced, allowing for operation at the optimal 2:1 ratio of pump to probe powers. While full analytical expressions can be found below, Fig. 3.1 outlines this trade-space, comparing standard stimulated and spontaneous Brillouin scattering to a stimulated Brillouin applying polarization pulling. Here, we assume a spontaneous Brillouin collection efficiency of $5.4x10^{-11}$ and stimulated Brillouin gain coefficient of $1.0x10^{-4}W^{-1}$ as typical values for

water. We assume a 10% duty cycle unless otherwise noted. Figure 3.1(a) demonstrates the basic advantage captured by polarization pulling, plotting shot limited SNR (in signal power) per ms of integration time vs. total average power, $\langle P_{probe} \rangle + \langle P_{pump} \rangle$. We assume the polarization sensitive detection rejects 98.5% of the probe power as used in the experiments below and is optimal at 10 mW detector saturation (see below for detailed analytical expressions). At low powers, the standard SBS using the ideal 2:1 ratio can outperform all other stimulated Brillouin based methods described here but it is fundamentally throttled by detector saturation (taken here to be 10 mW), such that, at best, it underperforms spontaneous Brillouin measurements by more than a factor of 10. The dashed line represents standard SBS with the power ratio allowed to vary but with the detected probe power fixed at the detector saturation level. Using higher ratios allows for higher detector limited SNR. However, by removing much of the initial probe power, the polarization pulling scheme can operate at much higher powers, using the ideal 2:1 ratio without saturating the detector, resulting in greater SNR. Figure 3.1(b) demonstrates how this advantage scales with duty cycle, assuming a 200 mW average power budget and with the detected power locked at 10 mW. Here the ratio of pump to probe power is allowed to vary for optimal SNR and, in the case of polarization pulling, the optimal rejection ratio is used at each point (letting more total light reach the detector as the peak power is reduced, while restricting more background probe light as greater peak power is available). The dot depicts the operating point from Fig. 3.1(a). Polarization pulling significantly outperforms standard SBS at low duty cycles. However, at higher duty cycles the advantage gets less pronounced as the polarization extinction ratio must be reduced until the two approaches

become almost equivalent and neither can outperform the spontaneous Brillouin scattering approach. Figure 3.1(c) shows how SNR varies as the detector saturation limit is adjusted for a 200 mW average power budget and 10% duty cycle with pump to probe power ratios and polarization rejection ratios set to optimal values. While the standard approach suffers at lower allowed detector power since it cannot operate at optimal power ratios, the polarization pulling scheme is approximately constant over this range as background light can be continuously reduced to compensate for lower detector saturation. Below, we show how a spectrometer, such as the one designed herein, compares to others in the prior art with respect to microscopy.

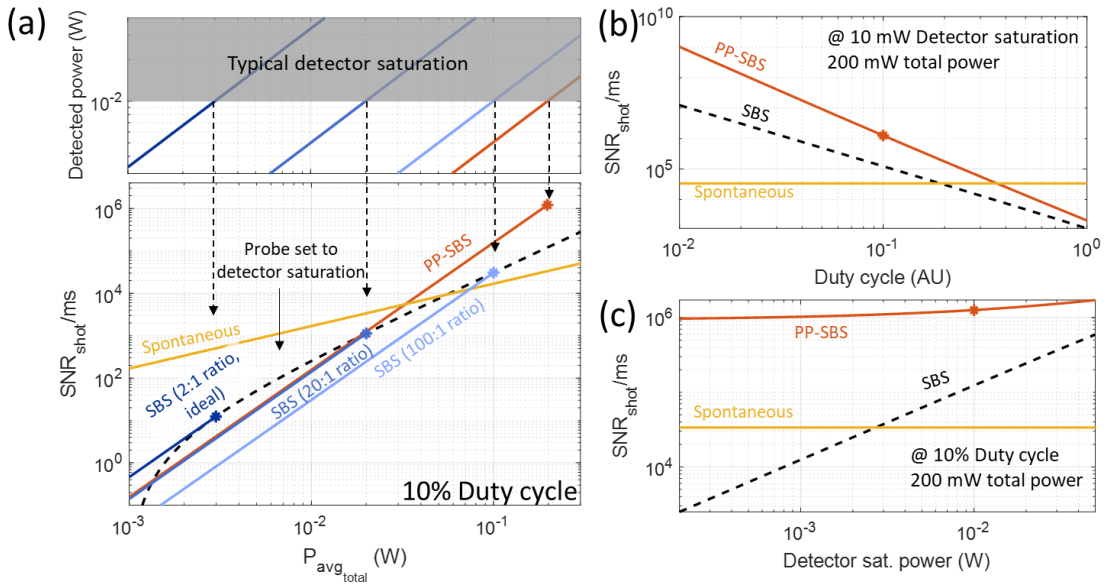

Fig. 3.1. (a) Demonstration of theoretical shot noise limited SNR (signal power) per ms and detected probe power vs total average power for various implementations of pulsed Brillouin assuming 10% duty cycle. The yellow line depicts spontaneous scattering (Spontaneous), blue lines show standard SBS with 3 different ratios of pump to probe power, and the orange line depicts polarization pulling (PP-SBS) approach with a fixed (ideal) 2:1 pump to probe power

ratio and with polarization sensitive detection rejecting a fixed 98.5% of the probe light. Standard SBS is limited by detector saturation (chosen here to be 10 mW) as shown in the upper plot with dots in the lower plot indicating this point. The dotted line in the lower plot shows the envelope of detector saturation as pump to probe ratio is varied which sets the probe power to the detector saturation. This limit throttles the standard SBS approach while the polarization pulling scheme can reject much of the original probe power. (b) shows the SNR per ms for SBS, PP-SBS, and Spontaneous vs. duty cycle for fixed total average power (200 mW) and operating at a fixed detector saturation power (10 mW). Lines depict optimal pump to probe ratio for each approach and at optimal polarization extinction for PP-SBS. (c) shows the SNR per ms for SBS, PP-SBS, and Spontaneous vs. detector saturation for fixed total average power (200 mW) and operating at a detector saturation power (10 mW) with a 10% duty cycle. Lines depict optimal pump to probe ratio for each approach and at optimal polarization extinction for PP-SBS.

3.1.1 Operating principle

In the standard SBS spectroscopy configuration shown in Fig. 3.2(a), counter-propagating pump and probe beams have the same polarization and overlap in the "SBS interaction region". In general, this interaction could take place at the focal point of a microscope, in an optical fiber, a waveguide, or other material of interest. The Brillouin gain spectrum is measured by sweeping the frequency of the pump (or the probe) and recording the amplified probe signal. In Fig. 3.2, we depict the implementation using pulsed pump and probe beams, although the same basic technique could be applied in CW. However, as discussed above, using pulses with a relatively low duty cycle enables better SNR without exceeding the damage thresholds related to average power and peak power. Finally, note

that the peak power of the probe pulse train must by low enough to avoid saturating the photodetector (the saturation power is labelled P_{sat} in Fig. 3.2). Figure 3.2 shows schematics of the standard SBS measurement and the polarization pulling scheme as well as the polarization components of the optical fields.

The polarization pulling scheme is shown in Fig. 3.2(b). In this case, the transmitted probe light passes through a PBS before reaching the detector. The PBS is aligned at an angle ϕ_{PBS} relative to the probe beam in order to reject most of the probe light, enabling the use of a much stronger initial probe beam without saturating the detector. In this scheme, the pump beam polarization is misaligned from the probe by an angle θ_{pump}, in order to "pull" the polarization of the amplified probe light towards the polarization of the pump (see the lower left inset in Fig. 3.2(b)). The amplified probe light is then preferentially transmitted through the PBS for detection. This approach can achieve higher SNR than a standard SBS measurement by enabling the use of a much stronger probe beam without saturating the detector. Below, we use an analytic model of the polarization pulling detection scheme to optimize the system configuration (e.g. the PBS angle ϕ_{PBS} and the pump polarization θ_{pump}) and estimate the potential performance improvement. We then experimentally validate this model using a fiber optic setup enabling us to compare a standard SBS setup with the polarization pulling scheme over a wide range of Brillouin gain.

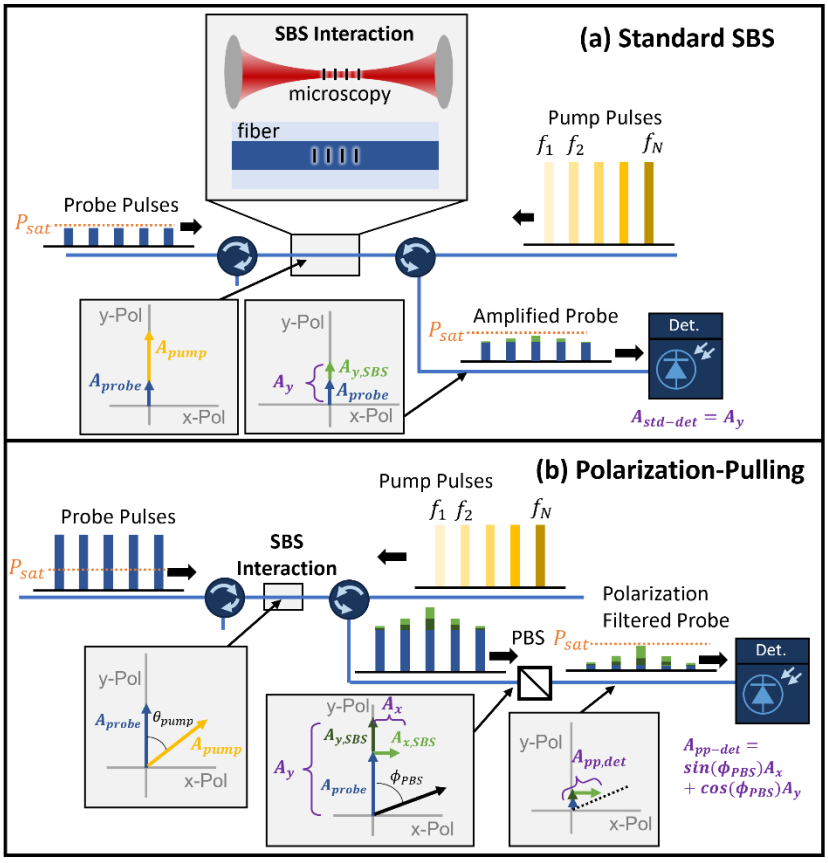

Fig. 3.2. Schematic depiction of (a) simplified Standard SBS and (b) Polarization Pulling detection schemes (PBS: polarizing beamsplitter, ϕ_{PBS}: the PBS transmission axis with respect to the probe polarization, θ_{pump}: the pump polarization with respect to the probe polarization). Shown in yellow are the pump pulses, in blue the probe pulses, and in green the Brillouin amplified probe. Inset field diagrams show the various linear-polarization components of the fields. Note that standard SBS measurements are taken with co-polarized pump and probe fields for maximal gain whereas in polarization pulling they are intentionally misaligned.

To model the SNR of Brillouin measurements obtained using the polarization pulling detection scheme, we need to calculate the detected "signal" level due to SBS amplification. To do this, we first assume that the probe field is aligned in the y polarization

and has an initial amplitude, A_{probe}, while the pump beam has amplitude A_{pump} with polarization that is rotated by an angle θ_{pump} with respect to the y-axis (as shown in the lower-left inset in Fig. 3.2b). After the SBS interaction, the probe field can be decomposed into x and y polarizations with amplitude A_x and A_y, where $A_x = A_{x,SBS}$ describes the Brillouin amplified field in the x polarization and $A_y = A_{probe} + A_{y,SBS}$ contains both the transmitted probe and the Brillouin amplified field component in the y polarization (see the lower-middle inset in Fig. 3.2b). We can model the polarization pulling effect due to the misalignment between the pump and probe polarizations by expressing A_x and A_y, which can be derived from the pulling expression in Ref. [74], as:

$$A_x = A_{x,SBS} = \sin(\theta_{pump})\cos(\theta_{pump})\, A_{probe}\,(e^{G_{SBS}/2} - 1) \tag{3.1a}$$

$$A_y = A_{probe} + A_{y,SBS} = A_{probe}\, e^{\cos(\theta_{pump})\, G_{SBS}/2} \tag{3.1b}$$

where G_{SBS} is the Brillouin power gain when the pump and probe polarizations are aligned (i.e. $G_{SBS} \equiv |A_y|^2 / |A_{probe}|^2$ at $\theta_{pump} = 0$). The $\sin(\theta_{pump})$ and $\cos(\theta_{pump})$ terms account for the reduction in Brillouin gain due to misaligning the pump and probe polarization (as $\theta_{pump} \to 90°$, $A_{x,SBS}$ and $A_{y,SBS} \to 0$). From these expressions, we see that the polarization pulling effect is most efficient (i.e. A_x is maximized) for $\theta_{pump} = 45°$. Note that these expressions can be applied to both the standard SBS scheme and the polarization pulling scheme by adjusting θ_{pump}.

In a standard SBS measurement with $\theta_{pump} = 0$, the detected probe field amplitude simplifies to $A_{std-det} = A_y = A_{probe}\, e^{G_{SBS}/2}$ since $A_x = 0$. We can then calculate the

detected "signal" power, $P_{std-signal}$, as the difference between the detected power when the pump is present, $P_{std-SBS}$, and the detected probe power in the absence of SBS, $P_{std-ref}$, as:

$$P_{std-signal} = P_{std-SBS} - P_{std-ref} \tag{3.2a}$$

$$P_{std-SBS} = A_{std-det} A^*_{std-det} \tag{3.2b}$$

$$P_{std-ref} = A_{probe} A^*_{probe} \tag{3.2c}$$

Finally, to facilitate comparisons with our experiments, we can convert this detected signal level to measured voltage as $V_{std-signal} = \left(R_{V/A}\mathcal{R}_{A/W}\right)P_{std-signal}$ where $R_{V/A}$ is the transimpedance gain in V/A and $\mathcal{R}_{A/W}$ is the detector responsivity in A/W.

In the polarization pulling scheme, the detected probe field after passing through the PBS can be expressed as $A_{pp-det} = \cos(\phi_{PBS})\, A_y + \sin(\phi_{PBS})\, A_x$. As in the standard SBS case, we can calculate the detected "signal" power in the polarization pulling configuration, $P_{pp-signal}$, as the difference between the detected power when the pump is present, P_{pp-SBS}, and the detected probe power in the absence of SBS, P_{pp-ref},:

$$P_{pp-signal} = P_{pp-SBS} - P_{pp-ref} \tag{3.3a}$$

$$P_{pp-SBS} = A_{pp-det} A^*_{pp-det} \tag{3.3b}$$

$$P_{pp-ref} = \cos^2(\phi_{PBS}) A_{probe} A^*_{probe} \tag{3.3c}$$

Under typical operating conditions where $G_{SBS} \ll 1$ (typically ~10^{-5}), $\theta_{pump} = 45°$, and ϕ_{PBS} is adjusted to provide reasonable extinction such that $G_{SBS} \ll \sin^2(\phi_{PBS}) \ll 1$ (typically 10^{-1} - 10^{-3}), equations 3.1-3.3 can be simplified to:

$$P_{pp-signal} \cong \sin(\theta_{pump}) \cos(\theta_{pump}) P_{probe}(G_{SBS}/2) \quad (3.3d)$$

Again, the measured signal level in the polarization pulling case can be converted to voltage as $V_{pp-signal} = (R_{V/A}\mathcal{R}_{A/W})P_{pp-signal}$.

3.1.2 Noise analysis

Here we present analytical expressions further describing this trade-space including other noise sources. Using equations 3.1-3.3, we can calculate the measured "signal" level for the standard and polarization pulling schemes as a function of Brillouin gain as well as the orientation of the pump polarization, θ_{pump}, and the PBS, ϕ_{PBS}. In order to estimate the SNR and the measurement uncertainty (or the acquisition time required to reach a desired uncertainty), we also need to estimate the measurement noise. We can describe the measurement noise in terms of the RMS voltage uncertainty, σ_V, during a measurement of an amplified probe pulse of duration τ. In the ideal case, σ_V will be dominated by shot-noise, σ_{V-shot}, although experimentally, noise from the photodetector, σ_{V-det}, or the analog to digital converter (ADC), σ_{V-ADC}, could also be significant, especially as $\phi_{PBS} \rightarrow 90°$ and the power reaching the detector is reduced. Other possible noise sources such as amplified spontaneous emission (ASE) and relative intensity noise (RIN) could be significant in some implementations but are not accounted for here. One way of reducing RIN is using a form of balanced detection, but this can significantly increase shot noise. In our model, we estimated the contribution from each of these noise sources using the following expressions:

$$\sigma_{V-shot} = R_{V/A}\sqrt{2qP_{det}\mathcal{R}_{A/W}/\tau} \tag{3.4a}$$

$$\sigma_{V-ADC} = \sigma_{V-ADC,0}/\sqrt{f_{ADC}\,\tau} \tag{3.4b}$$

$$\sigma_{V-det} = R_{V/A}\mathcal{R}_{A/W}P_{NEP}\sqrt{1/\tau} \tag{3.4c}$$

where q is the charge of an electron, P_{det} is the total optical power reaching the detector (e.g. $P_{det} = P_{pp-SBS} + P_{pp-ref}$), $\sigma_{V-ADC,0}$ is the RMS voltage uncertainty per sample of the ADC at a sample rate f_{ADC}, and P_{NEP} is the noise equivalent power of the photodetector. The total voltage uncertainty over a pulse length τ was given by summing each of these noise sources in quadrature. We can then calculate the SNR using the expressions for the signal level in voltage listed above as

$$SNR_{\tau} = \left[\frac{V_{signal}}{\sigma_V}\right]^2 \tag{3.5}$$

In the case of shot limited noise and under the typical operating assumptions described above, $SNR_{\tau-shot} \cong \left[\cos(\theta_{pump})\,P_{probe}(G_{SBS}/2)\mathcal{R}_{A/W}\right]^2/(2q/\tau) \propto P_{pump}^2 P_{probe}$. Finally, we use this SNR estimate to calculate the uncertainty in the measured Brillouin frequency as an amplitude spectral density (ASD_f) in units of $Hz/\sqrt{Hz}$, assuming quadratic fitting over the FWHM of the measured peak, as [75]:

$$ASD_f = \sqrt{\frac{3}{4}}\left[\frac{1}{\sqrt{SNR_{\tau}}}\right]\frac{\Gamma_B}{\sqrt{PRF/2}}\frac{1}{\sqrt{\Delta f_{scan}/\Gamma_B}} \tag{3.6}$$

where Γ_B is the Brillouin linewidth, PRF is the pulse repetition frequency, and Δf_{scan} is the bandwidth the pump is swept over to obtain a measurement of the gain spectrum. The $\sqrt{\Delta f_{scan}/\Gamma_B}$ term accounts for the trade-off between dynamic range and measurement

uncertainty, since measurements outside the Brillouin gain spectrum do not provide significant additional information. The leading $\sqrt{3/4}$ fraction assumes a quadratic fit of the peak and would negligibly change if Lorentzian fitting was used instead. Note that the frequency ASD is, to a good approximation, independent of the number of frequency steps taken across the scan bandwidth, as long as at least three frequency steps were taken within the Brillouin linewidth [75]. Of course, the number of frequency steps will still impact the minimum time required to complete a frequency scan and obtain a measurement, but this can be quite short (e.g. 10 μs in our experiments described below). The ASD can then be used to estimate the frequency uncertainty in a given measurement time, T, as $\sigma_f = ASD_f/\sqrt{2T}$ or the time required to obtain a measurement with a desired precision σ_f, as $T = (1/2)\left(ASD_f/\sigma_f\right)^2$ (assuming white noise).

Finally, we used these expressions to calculate the signal level and ASD obtained in the standard and polarization pulling schemes as a function of θ_{pump} and ϕ_{SBS}, as shown in Fig. 3.3. The Brillouin gain was set to $G_{SBS} = 2 \times 10^{-4}$. In these simulations, we selected detection parameters to match our experiments. Specifically, we assumed a photodetector with $\mathcal{R}_{A/W} = 1A/W$, $R_{V/A} = 700\,V/W$, $P_{NEP} = 10^{-12}W/\sqrt{Hz}$, and $P_{sat} = 1.4$ mW and an ADC with $\sigma_{V-ADC,0} = 0.5\ mV$ and $f_{ADC} = 1GS/s$. The pump and probe beams were both pulsed at a 10% duty cycle with a pulse duration τ=10 ns and $PRF = 1\ MHz$. The scan bandwidth was set to $\Delta f_{scan} = 2\Gamma_b = 60\ MHz$ (using the Brillouin linewidth for standard optical fiber).

In the standard SBS simulations, we set the peak probe power to 1.4 mW, as required to avoid saturating the photodetector. In the polarization pulling simulation, the peak probe power was set to 48.5 mW to avoid saturating the detector at the lowest ϕ_{PBS} considered. As shown in Fig. 3.3(a), the signal level in the standard case, shown in black, decreases monotonically with θ_{pump} (as expected, there is no advantage to misaligning the pump and probe polarization in the standard case). However, in the polarization pulling case, the signal level is maximized for $\theta_{pump} = 45°$ for each ϕ_{PBS} setting. We also found that the actual measured signal level in the polarization pulling case can be higher than in the standard case for $\phi_{PBS} < \sim 87.8°$. Of course, increasing the signal level by reducing ϕ_{PBS} also results in higher background probe power hitting the detector, which will increase the shot noise. To evaluate this trade-off, we can consider the ASD shown in Fig. 3.3(b). In the standard case, the ASD increases with θ_{pump}, as expected. However, in the polarization pulling case, we find that the ASD is minimized for $\theta_{pump} = 45°$ and can actually be a factor of ~10 lower than the ASD obtained in the standard case because of the higher, useable probe power. We also find that the minimum ASD is relatively constant for $\phi_{PBS} < \sim 87.8°$. In this regime, the measurement is shot-noise limited and adjusting the probe extinction at the PBS does not change the overall measurement precision. As $\phi_{PBS} \rightarrow 90°$, the signal and background probe light are both significantly reduced and the detector and ADC noise begin to dominate (see Fig. 3.3(c,d,e) for the impact of different noise sources at varying ϕ_{PBS}), resulting in the higher ASD noise shown in Fig. 3(b) for $\phi_{PBS} > \sim 89.3°$.

To summarize, these simulations indicate that the polarization pulling scheme is most efficient for $\theta_{pump} = 45°$. Somewhat surprisingly, high extinction at the PBS is not required and can actually make the measurement more sensitive to detector and ADC noise. Note that setting ϕ_{PBS} in the range of 83.1° to 87.8° corresponds to 18.4 to 28.3 dB of extinction, which is easily obtained with most commercial polarizers and polarizing beamsplitters. Crucially, this analysis also confirms that polarization pulling has the potential for significantly higher SNR than standard SBS measurements in applications where the power allocated to the probe beam is limited by the saturation threshold of the photodetector. As a result, polarization pulling could significantly accelerate Brillouin microscopy measurements since an improvement in ASD of 10× corresponds to a 100× decrease in acquisition time for the same measurement precision.

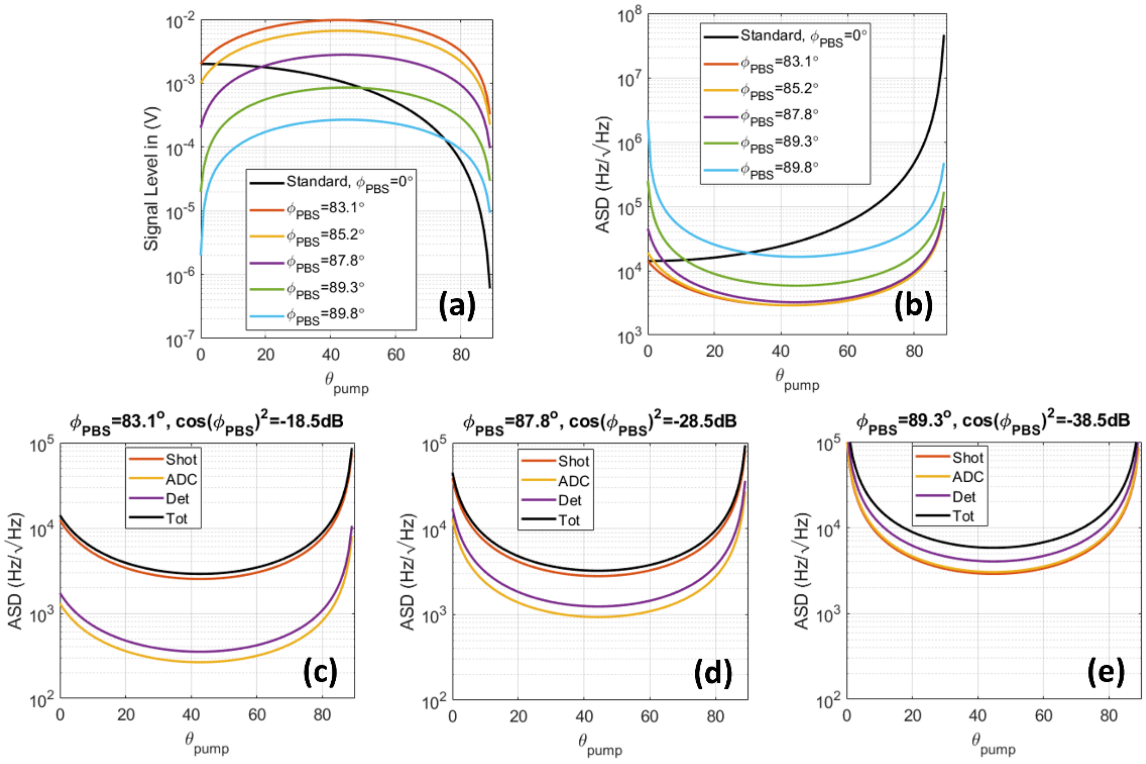

Fig. 3.3. Demonstration of noise model performance metrics. (a) The Brillouin amplified signal level and (b) ASD as a function of the angle between the pump and the probe beams. The colored lines indicate various extinction levels in the polarization pulling configuration. Notice at modest extinction, the ability of polarization pulling to achieve higher signal levels and thus lower ASD when the pump angle is roughly 45°. The black line represents the standard SBS signal level which is maximized when the pump and probe are co-polarized. (c-e) ASD due to various noise sources as a function of the angle between the pump and the probe beams across multiple extinction levels.

3.2 Experimental demonstration

In order to validate our model and confirm that polarization pulling does in fact result in higher SNR measurements, we conducted experiments using a fiber optic platform where the Brillouin gain can be easily varied over several orders of magnitude. As shown in Fig. 3.4, both the pump and probe arms were seeded with the same narrowband laser (kHz linewidth, RIO Orion) operating at ITU Channel 32 (193.2 THz). Using the same seed laser for the pump and probe reduces the sensitivity to laser frequency noise, particularly in spectroscopy applications where the pump and probe arms can be path matched. Along the upper path, an electro-optic modulator (EOM) was used to generate the frequency shifted pump pulses with a duration of 100 ns and a repetition period of 1 μs (10% duty cycle). The EOM was driven in carrier suppressed mode and the frequency of the 100 ns bursts increased in 10 steps from 10.81 GHz to 10.87 GHz, covering a 60 MHz band corresponding to twice the Brillouin linewidth in the fiber ($\Gamma_B \sim 30\ MHz$). The system

completed a frequency scan every 10 μs. Using a high-speed AWG (Tektronix AWG70001B) to drive the EOM in this way provides a versatile platform with easily adjustable pulse duration, duty cycle, frequency step size, and scan range.

After the EOM, light was directed to a tunable bandpass filter (Santec OTF-980) which selected the upper sideband. An Erbium doped fiber amplifier ($EDFA_1$) was then used to control the power of the pump pulses in order to adjust the SBS gain. A 100 GHz-wide wavelength division multiplexing (WDM) filter was positioned after the EDFA to suppress amplified spontaneous emission. The pump pulses were then directed through a polarization controller (PC_1) before coupling into the SBS interaction region through a fiber circulator. The SBS interaction region consisted of 2 m of single mode optical fiber (SMF-28 Ultra) held straight at uniform tension to ensure a consistent Brillouin frequency and to minimize polarization rotation within the 2 m segment of fiber (note that polarization dispersion in SMF-28 Ultra results in ~200 nm in path mismatch between polarization states in this case). In the probe path, the seed laser was amplified by $EDFA_2$, directed through another WDM filter, and passed through a polarization controller (PC_2) before entering the interaction fiber through a circulator. The Brillouin amplified probe light was then split between a standard SBS detection port (consisting of a variable attenuator and a detector) and the polarization pulling detection port (consisting of a fiber-coupled polarizing beamsplitter and a detector). In both cases, we used 125 MHz photodetectors with a saturation power of ~1.4 mW (Teratec, TTI-525) and the detected signal was digitized using a 1 GS/s ADC.

Note that in these experiments, we used a CW probe for simplicity, rather than the pulsed probe shown in Fig. 3.2. Since photodamage was not a concern using the fiber sample, this allowed us to demonstrate the principle of polarization pulling without requiring an additional modulator. In the future, pulsing the probe at the same 10% duty cycle as the pump would reduce the average power in the SBS interaction region (to minimize photodamage) without impacting the measurement SNR.

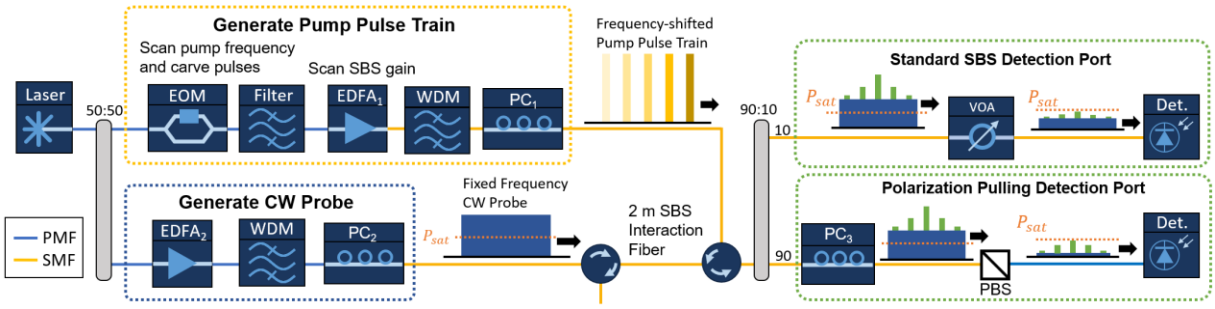

Fig. 3.4. Diagram of the experimental setup used in this work. The upper path was used to generate the pulsed pump train. The lower path generates the CW probe beam. When operating with the standard SBS port, the polarization controls in the pump and probe paths (PC_1 and PC_2) are used to co-polarize the two beams, maximize the Brillouin gain in the 2 m interaction fiber. To use the polarization pulling port, PC_3 is adjusted to avoid saturating the detector and PC_1 is adjusted to maximize the signal level, setting the pump polarization to ~45° relative to the probe. Note the solid blue lines indicate polarization maintaining fiber (PMF) whereas solid orange lines indicate single mode fiber (SMF).

3.2.1 Brillouin measurements in optical fiber

First, we performed a series of measurements using the standard SBS port to quantify the baseline measurement uncertainty over a wide range of Brillouin gain values. A variable

optical attenuator (VOA) was used to set the detected probe power just below the saturation level of the photodetector. In practice, rather than using a VOA, a lower initial power probe should be used to minimize power in the SBS interaction region. However, positioning the VOA in the SBS detection port path, rather than, e.g., reducing the gain on $EDFA_2$, does not impact the measurement SNR on the standard port and allows us to more easily switch between the two detection ports. We then aligned the polarization of the pump and probe beams using PC_1 and PC_2 to maximize the measured gain on the standard port detector. At each pump power setting, we recorded the transmitted probe beam for 10 ms, providing 1000 measurements of the Brillouin gain spectrum (each measurement is completed during a 10 μs frequency scan). We applied a Lorentzian fit to each 10 μs measurement to estimate the Brillouin frequency and calculated the ASD [76]. We also extracted the gain and measured signal level (using the definition in Eq. 3.2) for comparison with our model. Note that at low gain ($G_{SBS} < 10^{-3}$), the standard port does not have sufficient SNR to provide a reliable measurement of the Brillouin frequency shift using a single 10 μs frequency scan. To obtain a more reliable measurement at these gain values, we first averaged 10 sequential frequency scans before performing the Lorentzian fit and updated the ASD calculation to account for a 10x increase in the effective time required to complete a frequency scan.

We then performed a series of measurements over the same range of pump powers using the polarization pulling setup. In this case, we first adjusted PC_3 so that the probe power transmitted through the PBS and reaching the polarization pulling detector was just below the saturation level. Based on the measured probe power of ~77 mW exiting the interaction fiber, this corresponded to a $\phi_{PBS} \sim 83°$ and attenuation at the PBS of ~19 dB. We then

adjusted the pump polarization using PC_1 to maximize the signal level due to Brillouin amplification observed on the polarization pulling detector. Based on the model presented above, this corresponds to $\theta_{pump} \sim 45°$. We then recorded a series of measurements at the same pump power settings used on the standard port. For each pump power, we again recorded the transmitted probe for 10 ms and applied a Lorentzian fit to the gain spectrum obtained from each 10 μs frequency scan. The data obtained with an AC coupled detector during a typical 10 μs scan is shown in Fig. 3.5(a) at a pump power that corresponded to $G_{SBS} \sim 1.4 \times 10^{-4}$ on the standard port. We first applied a 100 ns moving average to the raw data acquired at 1 GS/s, to match the 100 ns pump pulse duration. We then selected the "signal" due to Brillouin amplification based on the definition in Eq. 3.3 as the difference between the measured voltage at the center of each pump pulse and the average background voltage level. The resulting gain spectrum was then fit with a Lorentzian, as shown in Fig. 3.5(b). This procedure was repeated for 1000 frequency scans at 9 pump powers, corresponding to G_{SBS} in the range of 10^{-4} to 10^{-2}. Unlike the standard SBS port, the measurements on the polarization pulling port had sufficient SNR to reliably extract the Brillouin frequency in a 10 μs frequency scan down to the lowest G_{SBS} measured of ~9×10^{-5}. For example, the measurement uncertainty obtained in a 10 μs scan at $G_{SBS} \sim 1.4 \times 10^{-4}$ was ~1 MHz, corresponding to ~1/30th of the Brillouin linewidth in optical fiber.

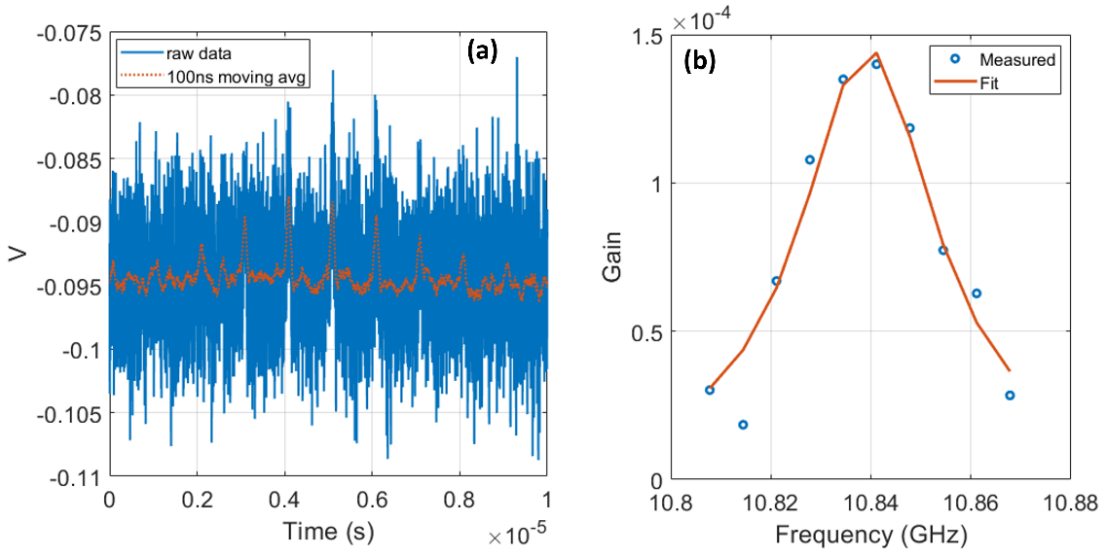

Fig. 3.5. (a) The raw data recorded in the polarization pulling port in 10 μs representing a single frequency scan across 60 MHz in 10 discrete steps using 100 ns pump pulses at a 10% duty cycle. Note that the AC coupled detector had a voltage offset of -0.094 V. (b) The gain spectrum measured on the polarization pulling port normalized to G_{SBS} measured using the standard SBS port at the same pump power.

3.2.2 Experimental validation of modeled signal level characterization

We then compared the measurements obtained on the standard and polarization pulling ports with our model. The measured signal levels obtained as a function of G_{SBS} are shown in Fig 3.5(a). This measurement shows excellent agreement with our model over the full range of G_{SBS} and confirms that the polarization pulling scheme is able to obtain a higher measured signal level, in agreement with the prediction shown in Fig. 3.3(a). We then compared the measured frequency uncertainty ASD over the same range of G_{SBS}, as shown in Fig. 3.3(b). We found a good agreement with the model for gain below ~10^{-3}. At higher

gain, reflected pump light due to Rayleigh backscattering and/or imperfections in the fiber circulators began to degrade the measurement obtained on the polarization pulling port. In the future, a narrowband spectral filter could be used to reject pump light before it reaches the detector [33,34,41]. Nonetheless, this measurement confirmed that the polarization pulling detection scheme can provide a ~10x reduction in ASD in low-gain measurements where the probe power is limited by the detector saturation threshold.

Finally, we compared the measured signal level and ASD as a function of θ_{pump} at a gain of $G_{SBS} = 2 \times 10^{-4}$, as shown in Fig. 3.6(c,d). Again, the signal and ASD agree well with our model and indicate that we are operating near the optimal conditions for a polarization pulling measurement.

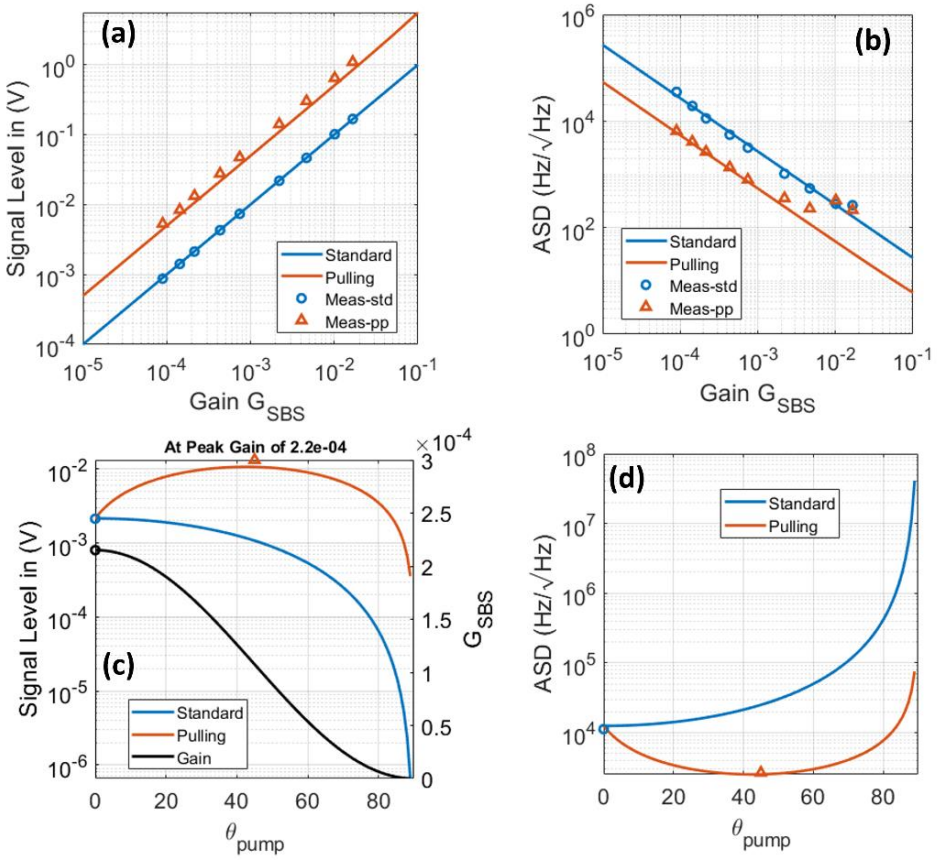

Fig. 3.6. Demonstration of experimental results compared with our noise model. (a) The Brillouin amplified signal level and (b) ASD as a function of gain. At high pump powers, back-reflected pump light increases the measured ASD. (c) The Brillouin amplified signal level in the respective optimal conditions compared to the model. Gain, in black, corresponds to the right Y-axis title and is marked at the standard SBS peak gain. (d) Measured ASD in the respective optimal conditions compared to the model with a ϕ_{PBS}~83°.

3.3 Comparative uncertainty targets

The polarization pulling detection scheme presented in this work is particularly well-suited for Brillouin microscopy measurements in the biological regime. Brillouin microscopy has traditionally relied on spontaneous Brillouin scattering; however, in recent years, SBS has been proposed due to its potential for increased efficiency and reduced measurement times. In practice, SBS has provided only a modest speed-up since damage thresholds in biological materials limit the pump and probe power, restricting SBS measurements to the low-gain regime (10^{-5} to 10^{-4}). Recent work has shown that pulsing the pump and probe lasers could partially alleviate this concern [40,41] by maintaining a fixed average power while increasing the peak power. However, pulsing the probe can result in peak powers that are well beyond the saturation threshold of commercially available photodetectors. This makes it difficult to use the optimal, ~2:1 distribution of pump to probe power. The polarization pulling scheme presented here was designed to address this restriction by discarding most of the background probe light before it reaches the detector.

In this chapter, we presented an analytic model showing that this approach has the potential for a >25x improvement in SNR compared to standard SBS measurements in typical Brillouin microscope conditions, assuming commercially available detectors with saturation power in the 1-20 mW range. We then experimentally validated this model using a fiber optic platform that allowed us to easily vary the Brillouin gain over several orders of magnitude. Although the fiber platform has significant differences from a biological sample, we can normalize for these distinctions to compare the polarization pulling measurements presented in this work to recent SBS measurements in biological microscopy applications. First, the Brillouin linewidth in optical fiber of ~30 MHz is ~10× narrower than in most biological samples, as well as water, which has a linewidth of ~300 MHz and is commonly used to benchmark biological Brillouin microscopy systems. As shown in Eq. 3.6, the measurement uncertainty is proportional to the Brillouin linewidth. As a result, we cannot directly compare the measured frequency uncertainty in fiber and water but need to normalize by the Brillouin linewidth. Second, most Brillouin microscopes report the acquisition time required to obtain a biologically relevant accuracy, typically ~$\Gamma/30$ [11,77,78]. We therefore converted the measured ASD shown in Fig. 3.6(b) to the time required to obtain a measurement with a normalized uncertainty of $\Gamma/30$ as $t_{\Gamma/30} = \frac{1}{2}\left(ASD_f/\sigma_{\Gamma/30}\right)^2$, where the target uncertainty $\sigma_{\Gamma/30} = 1MHz$ for optical fiber. Third, as shown in Eq. 3.6, the uncertainty also depends on the frequency scan bandwidth. Most biological measurements use a scan bandwidth of ~2Γ [33,34,40,41], which matches the normalized scan bandwidth used in this work. Finally, since we are comparing measurements with different materials, interaction lengths, and pump powers, we can

compare $t_{\Gamma/30}$ as a function of Brillouin gain, which dictates the measured signal level. As discussed above, for a fixed average power, using pulsed pump and probe beams will increase the measured gain, SNR, and reduce the required measurement time for a fixed precision [40]. To compare measurements performed at different duty cycles, we normalize by the $duty-cycle \times G_{SBS}$ product. This normalization implies that a sample that provides a CW gain of 10^{-5} at the maximum allowed average power of 200 mW could be probed at a 10% duty cycle to obtain a peak gain of 10^{-4}. The $t_{\Gamma/30}$ at a given $duty-cycle \times G_{SBS}$ product then allows us to compare the acquisition time (pixel dwell time) required to obtain an accuracy of $\Gamma/30$ for a fixed material, interaction length, and average power.

3.3.1 State-of-the-art stimulated Brillouin scattering spectrometer comparison

We applied this normalization to both the standard SBS and polarization pulling measurements reported above in Fig. 3.6. As shown in Fig. 3.7, the standard SBS measurements obtained in fiber agree relatively well with a series of recent experimental measurements recorded in water over a range of $duty-cycle \times G_{SBS}$ products. In contrast, the polarization pulling measurements shown in Fig. 3.7 show a ~100× shorter acquisition time compared to the standard SBS measurements. For example, at a $duty-cycle \times G_{SBS}$ product of 1.4×10^{-5}, the polarization pulling scheme achieves the target frequency uncertainty of $\Gamma/30$ in just 10 μs (i.e. a single frequency scan in the experiments presented here), compared to Refs. [33,34] which required ~3 ms to achieve the same

uncertainty using standard SBS detection. This would represent a dramatic improvement in image acquisition time in a Brillouin microscopy application.

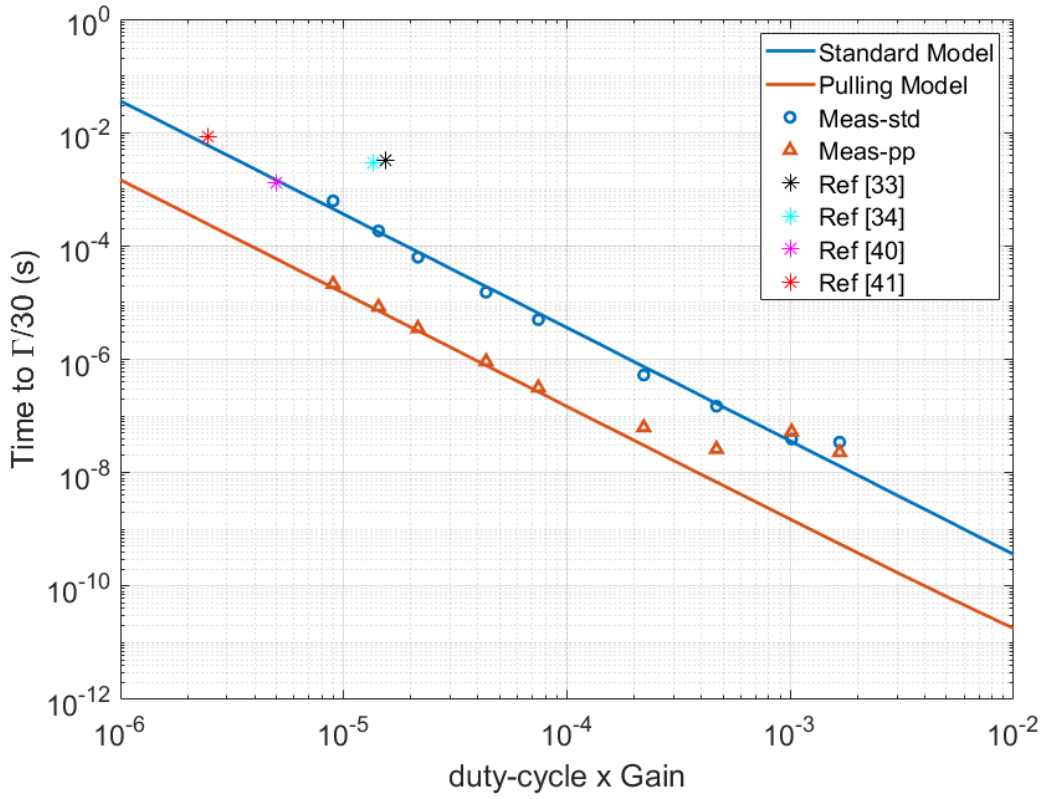

Fig. 3.7. Measured standard and polarization pulling SBS results compared to our noise model and a few recent SBS microscopy publications, as denoted in the legend, on normalized axes describing the measurement time needed to achieve a frequency uncertainty of $\Gamma/30$ versus the product of duty-cycle and gain. Of note, Refs. [33,34] both operate with a CW pump and probe whereas Refs. [40,41] uses pulsed pump and probe beams. Polarization pulling offers a significant speed-up compared to current Brillouin spectrometers.

3.4 Conclusion

In this chapter, we introduced a polarization pulling based SBS detection scheme. This technique separates the Brillouin amplified light from the background probe light, enabling the use of a strong probe beam without exceeding the detector saturation threshold. We developed an analytic model of the polarization pulling detection process which indicated that this approach could provide a significant increase in SNR compared to a standard SBS detection scheme using standard photodetectors with saturation thresholds in the 1-20 mW range. We experimentally validated this model using a fiber optic platform, confirming that the polarization pulling technique can provide a >25× improvement in SNR. Finally, we analyzed how this detection scheme could impact Brillouin microscopy measurements in the low-gain regime, indicating the potential for a >25× increase in imaging speed.

Chapter 4: Development of a custom laser source for pulsed stimulated Brillouin scattering microscopy

4.1 Optimal source parameters for Brillouin microscopy

4.1.1 Pulse duration considerations

The first of the laser parameters we can optimize is the pulse duration. If we refer back to Eq. 1.29(a), we know that the Brillouin gain of the transmitted probe beam is dependent on the intensity of the pump beam as well as the interaction length and the gain factor. The intensity of the pump beam can be understood as: $I_{pump} = P_{pump,peak}/A$, where A, for microscopy, is given from the beam waist area of the microscope and $P_{pump,peak}$ is the peak power of the pump beam. The interaction length in the gain equation specifically for microscopy is limited to the diffraction length of the focused laser beam: $L = 2\pi\omega_0^2/\lambda$. With this description, it is evident that Brillouin gain is directly proportional to the peak pump power, thus employing techniques to increase the peak pump power will result in higher Brillouin gain and better SNR.

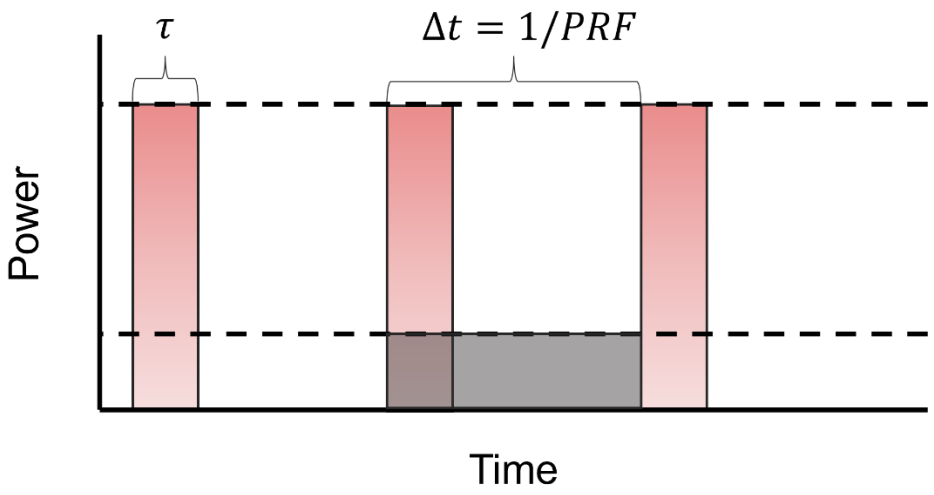

Fig. 4.1. Schematic of pulsed laser parameters.

Pulsing a laser source increases the peak power of the beam, see Fig. 4.1; therefore, using pulsed pump lasers increases the Brillouin gain experienced by the probe beam. Short pulse durations have high peak powers because the pulse energy is distributed over a short time frame. It might seem as if you could make the pulse duration arbitrarily short in order to have arbitrarily high peak power (an extremely high gain), but this is not possible in Brillouin for two reasons: 1) if we had extremely high peak power, this would mean we have extremely high instantaneous power in the pulse causing what is referred to as laser ablation [79,80] of the sample and 2) if the pulse duration was much shorter than the lifetime of the acoustic wave (for biological material ~1ns), the Brillouin efficiency will be greatly reduced. For these reasons, there is an optimal regime where Brillouin efficiency is maximized; nanosecond regime pulse durations satisfy these constraints as it is long enough to maintain a transform limited bandwidth narrower than the Brillouin linewidth (which is roughly 200MHz), and it must be as short as possible to achieve high Brillouin

gain ($G \propto P_{pump,peak} \propto 1/\tau$). Experimentally, nanosecond pulses can be created with either AOMs or EOMs and will be discussed below.

4.1.2 Pulse repetition frequency considerations

We have discussed the importance of optimizing the pulse duration for optimal Brillouin efficiency, but another parameter that ought to be evaluated is the pulse repetition frequency (PRF). Specifically in biological applications, photodamage imparted to the cells is of great interest[8] and can result in two ways: 1) thermal damage and 2) ablation damage. Thermal damage to cells arises from the absorption of light which can produce chemical changes and heat [19,20]. This mechanism of damage is mediated by the average power delivered to the sample during measurement. In CW SBS, where there is no PRF to consider, the average power has been kept to below ~250mW and has not induced significant damage [33,34]. One of the key benefits when using pulsed lasers is they reduce the average power on the sample [40,41]. As depicted in Fig. 4.1, average power of a pulse laser is defined as: $P_{avg} = E/\Delta t = E * PRF$, where E is the pulse energy which is spread over the pulse period (Δt). High PRFs correspond to high average power and thus the potential for thermal damage. If thermal damage is a concern, as it is in biological applications, lowering the PRF of the pulsed laser will reduce the average power on the sample. As with pulse duration, this cannot be arbitrarily small. When low PRFs are used,

[8] Naturally, you do not want to perturb the biological sample in any way that would compromise the mechanical measurement and/or damage the sample.

the peak power increases; $P_{peak} = \frac{P_{avg}}{\tau * PRF}$, where the product of pulse duration and PRF is defined as the duty cycle. We know that high peak powers are desirable in Brillouin because of the direct relationship between gain and peak power; however, in this condition, the second mechanism of damage to the sample can be a problem, ablation damage from instantaneous energy delivery from the pulse [81]. Recently, ablation damage has been the focus of much research in ultrashort laser pulses in biological material because of the widespread use of femtosecond lasers in Lasik surgery [79] and multiphoton imaging of tissues [80]. Additionally, using low PRFs can also limit the measurement rate of pulsed SBS. For example, if we want to take a Brillouin measurement with a 100ns pulse duration and 1μs period (a 10% duty cycle) across twice the Brillouin linewidth ($2\Gamma_B$) sampled with 10 frequency steps, one spectral measurement can be taken in $1\mu s * 10\ freq\ step = 10\mu s$. If we were to increase the period, thus lowering the PRF, to 2μs, we would double the time it would take to acquire a full spectrum if we used the same number of frequency steps: $2\mu s * 10\ freq\ step = 20\mu s$. Again, an optimal range is presented for Brillouin measurements: a PRF too high will result in thermal damage whereas one too low will cause ablation and spectral measurement time limits. Roughly MHz PRFs avoid damaging the biological samples by keeping peak powers below ~5W and average powers below ~250mW. Beyond photodamage constraints, keeping powers below these limits also ensures that the Brillouin shift is not corrupted via heating of the sample since Brillouin is highly temperature dependent [17,34,82].

4.2 Experimental design

4.2.1 Pulsed SBS laser in Master Oscillator Power Amplifier (MOPA) arrangement

Our experimental setup, see Fig. 4.2, starts with a narrowband seed laser (~100 kHz linewidth, Toptica DL-pro) which is locked at an ^{85}Rb absorption peak using a vapor-based locking module. Resulting in a nominal laser wavelength of 780.24nm (384.231 THz) at ~40mW which is then split 50:50 into both the pump and probe arms. Using one laser to seed both arms instead of two results in less laser frequency noise. Along the upper probe path, an EOM driven by radio frequency (~GHz) periodic voltage signals is operated in double-sideband carrier suppressed (DSB-SC) modulation mode to create sidebands off the nominal laser frequency. This process is explained in greater detail below. After the first EOM, the beam, which now contains multiple frequency components, is directed to a temperature controlled fiber bragg grating (FBG, TeraXion). The FBG has an 18.8GHz bandwidth and can be tuned (over a range of ~20GHz) using a temperature control to select the upper sideband (rejecting the lower sideband and nominal laser frequency). The FBG has isolation >35dB for out-of-band mean isolation of the nominal laser frequency and lower sideband outside of the narrow bandwidth tune range. This can be set by sending in the nominal laser frequency and tuning the bandwidth a few GHz beyond the point where the nominal laser is rejected, or the output could be viewed on a fiber-based wavelength meter. Next, the probe is sent to a second EOM for pulse carving of ~ns bursts of increasing frequency in 10 steps. The duration of the pulses, the duty cycle, frequency step size and number, and scan range are all customizable depending on the material under test. The pulses are then amplified using a fiber coupled amplification unit (Toptica Boosta) before

being sent through a polarization controller and isolator (if needed) to the material under test. The amplifiers used here are semiconductor tapered amplifiers which are more common in the visible wavelengths than rare-earth doped fiber-based amplifiers, such as the erbium doped fiber amplifiers used in Chapter 3, which require pump sources to excite the ions to amplify via stimulated emission. Tapered amplifiers also offer smaller gain bandwidths than fiber-based amplifiers. The transmitted probe can then be analyzed in a standard SBS or polarization pulling SBS detection port consisting of a variable optical attenuator (VOA) and a detector (Terahertz Tech., TIA-525).

Meanwhile, in the pump arm, the other partition of the seed laser is sent through another EOM to carve the pump pulse train. The pump pulse train is also amplified by a fiber coupled amplification unit (Toptica Boosta) and goes through a polarization controller before coupling into the SBS interaction region. It can be useful to pick off portions of the two beams for characterization and proper timing.

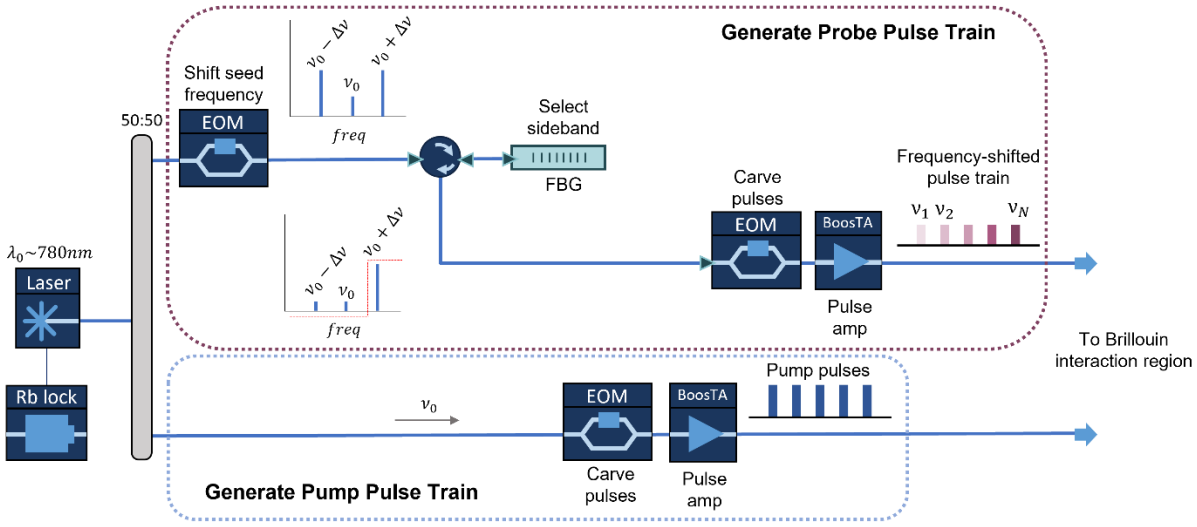

Fig. 4.2. Diagram of the pulsed SBS microscopy laser. The frequency-locked seed laser is split 50:50 between two paths: the upper path was used to generate the pulsed, frequency swept probe train while the lower path generates the pulsed pump train. A temperature-controlled fiber grating (FBG) is used to suppress the nominal laser frequency as well as the lower sideband.

The various electrical components used in this setup are shown in Fig. 4.3. In order to synchronize the timing of the two pulse trains with the frequency shifting, one output of AWG_2 (Keysight 33500B) triggers the pulse trains driven by a fast AWG_1 (Zurich HDAWG). This fast AWG_1 has a sampling rate of 2.4 GSa/s and two internal oscillators which is sufficient to generate the two ~ns pulse trains at MHz PRFs and to arbitrarily control their relative delays. Due to optical path mismatches of the two arms, time delays, albeit small, can be added to ensure the pulses are fully overlapped in the Brillouin interaction region. The smallest pulse duration that can be achieved (running the EOM in switching mode) using this AWG is 32 samples or 13.3ns. The maximum output voltage is 5V which is another critical factor when considering driving EOMs for pulse generation. This topic is expanded upon below when discussing pulse generation. The pulse carving EOMs are also DC biased to achieve good modulation depth of the optical pulses.

Along with trigger synchronization, AWG_2 provides the voltage ramp for the frequency shifting EOM. The maximum voltage output of this AWG is 5V so the largest voltage ramp that it can send to the voltage controlled oscillator (VCO) is 0-5V. The VCO converts a DC voltage signal to a radio frequency periodic signal. A VCO is an electronic oscillator whose output frequency is controlled by the input voltage level. VCOs typically

are comprised of an active device (in this case transistor) and the tuning range is adjusted by varying either the capacitance or inductance to achieve tuning. The VCO chosen here uses a variable capacitor whose capacitance can be tuned via the applied input voltage. This in turn alters the resonant frequency of the LC circuit and subsequently the output oscillation frequency of the VCO: $\nu_{out} = \frac{1}{2\pi\sqrt{LC}}$. The one chosen for this setup provides output in the GHz range suitable for creating GHz frequency shifted sidebands to the nominal laser frequency. Sidebands to the nominal laser frequency are created via DSB-SC modulation of the EOM. When EOMs are driven with periodic signals such as this, they add frequency components to the laser beam passing through the modulator, e.g. sending a 5GHz sinewave to an EOM creates sidebands to the nominal laser frequency at -5GHz and +5GHz. Biasing the EOM running in DSB-SC mode can be done to improve the efficiency of the conversion to the sidebands. It should be noted that higher order sidebands are also created but are significantly lower power compared to the sidebands and nominal laser frequency. As the voltage sent to the VCO (V_{tune}) is scanned from 0-5V, the VCO provides RF signals from ~3.8GHz to ~5.4GHz; however, a bias tee can be included to add a DC bias (from AWG_3) to the ramp which allows for more control over the scan range as well as extended accessibility to higher frequencies >6GHz.

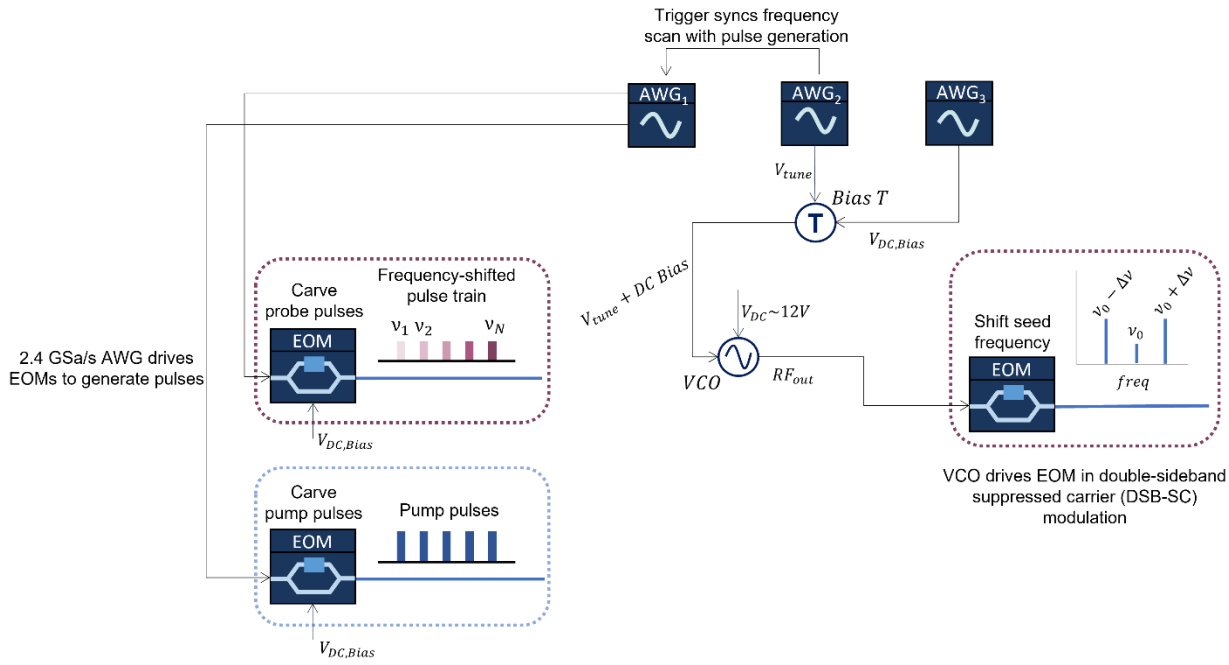

Fig. 4.3. Diagram of the electronics used in pulsed SBS microscopy laser. A high definition (2.4 GSa/s) arbitrary waveform generator (AWG) was used to carve both pump and probe pulses. The second AWG sends a voltage ramp to the voltage controlled oscillator (VCO) which is separately biased with another AWG and a bias T. This AWG also triggers the first AWG to begin the pulse trains. The VCO converts the voltage ramp into a radio frequency (RF) alternating current signal (~GHz) that drives the frequency shifting EOM in double-sideband suppressed carrier (DSB-SC) modulation. Various other sources of direct current (DC) voltage signals are excluded from the schematic.

4.2.2 Frequency shifting bandwidth control

Experimentally we can visualize the DSB-SC modulation by coupling the EOM output to a fast photodetector and a signal analyzer (Keysight CXA N9000B). Modern RF signal analyzers leverage a combination of analog and digital signal processes in order to analyze

high frequency (>GHz) signals. The analog front-end of these systems use internal local oscillators and mixers to down-convert the RF signal to lower intermediate frequencies (IF) which are more easily processed. This internal sweeping is done digitally and depends on the frequency range of interest; linear sweeps are used for smaller ranges while logarithmic sweeps are used for wide ranges. The digital back-end, once IF signal is converted to a digital signal using an analog-to-digital converter (ADC), goes through various digital processing steps such as digital filtering and fast Fourier transforms (FFTs) to analyze the signal. The one chosen for our signal analysis is capable out to ~13.6GHz, more than enough to analyze the ~5GHz shifts required for Brillouin measurements in biological samples. The beat frequency between the nominal laser frequency and the sidebands can be measured as well as the beat between the upper and lower sidebands. This is a useful way to monitor the frequency scan range being created and can be used to tune the output based the voltage ramp being sent to the VCO (V_{tune}) and the voltage bias.

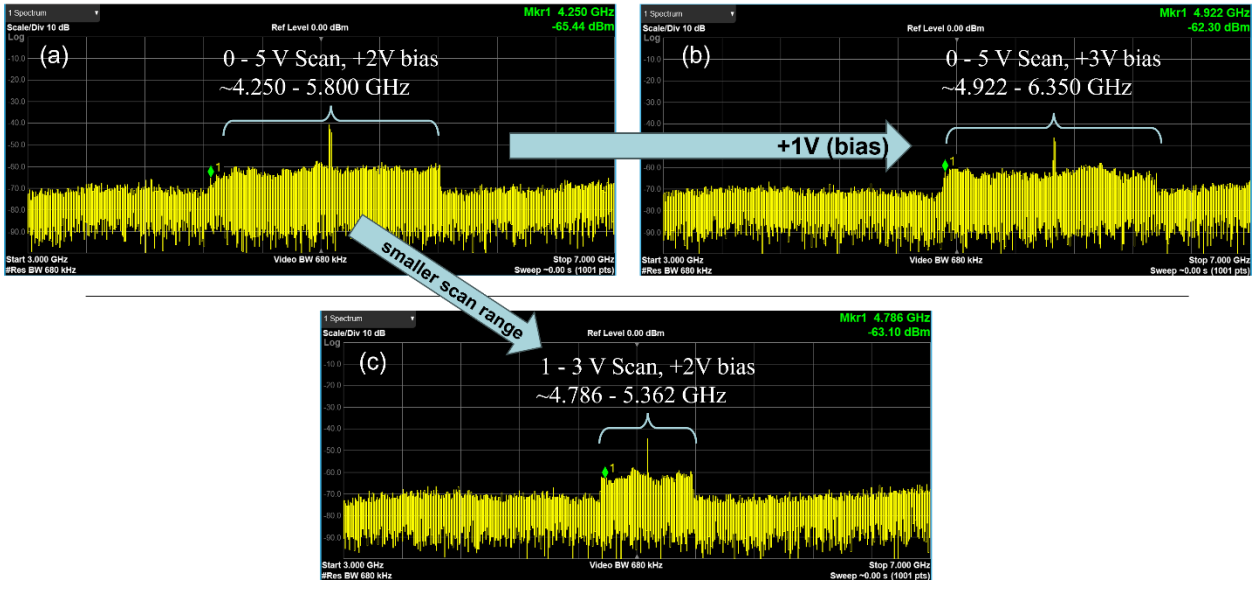

Fig. 4.4. The measured frequency scan range using the system described above for wide scan ranges. (a) The approximate frequency scan range suggested for measuring biological samples; centered ~5GHz using the typical scan range reported in most Brillouin microscopy literature ~4GHz-6GHz. (b) Increasing the bias voltage of the voltage ramp sent to the VCO repositions the frequency scan range accordingly. This can be used to simply move the frequency scan range to reach higher frequency ranges inaccessible with just a 0-5V ramp. This can also be a useful tuning lever when trying to search for a material's Brillouin shift not known *a priori*. (c) Decreasing the voltage ramp range shortens the frequency scan bandwidth. The measured values acquired on the signal analyzer correspond to the optical beat frequency between the nominal laser frequency and the sidebands created by the frequency shifting EOM.

Figure 4.4 demonstrates how the frequency scan range can be tuned for wide scans. For SBS microscopy, it is typical to use (2GHz wide) scan ranges between ~4GHz and ~6GHz for measurements of biological samples. As such, a frequency scan range appropriate for these measurements can be created by scanning V_{tune} from 0 to 5V with a +2V bias as shown in Fig. 4.4(a). For materials with higher Brillouin shifts, a larger voltage bias can be applied to reach frequencies >6GHz as shown in Fig. 4.4(b). Adding a voltage bias to the ramp does impart a slight nonlinearity, especially at higher voltages, in the scan range and should be taken into account when determining the corresponding frequency bandwidth. This is not really a problem with small scan ranges but does become apparent with wider scans (>1GHz). A smaller scan range is shown in Fig. 4.4(c) which corresponds to a bandwidth of ~700MHz which is approximately 2 times the linewidth of water at 780nm.

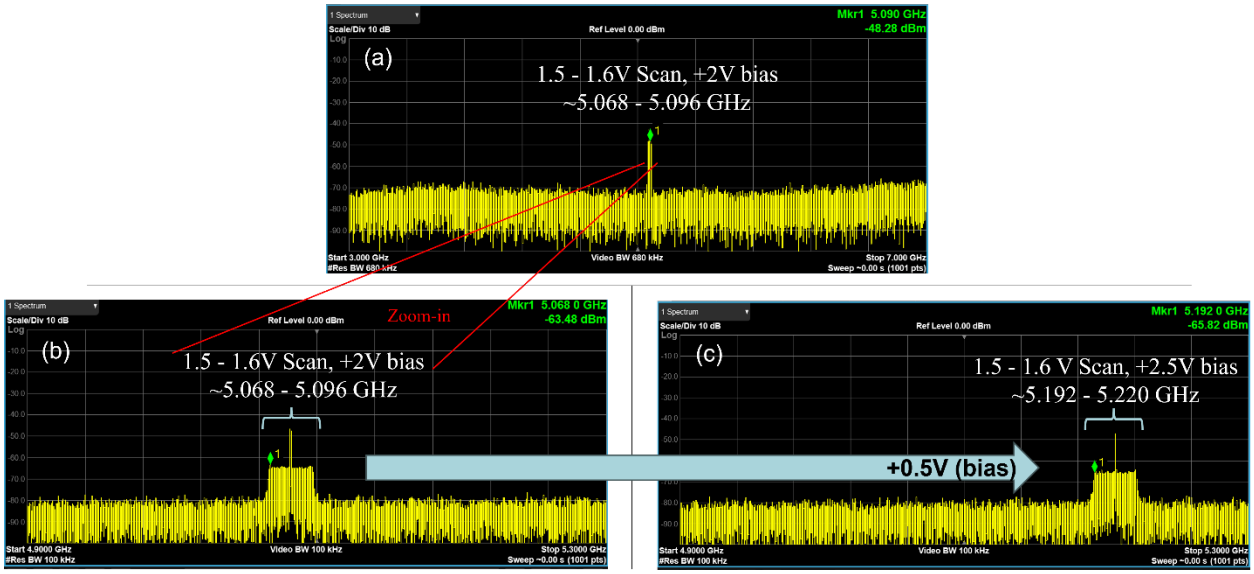

Fig. 4.5. The measured frequency scan range using the system described above for small scan ranges. (a) The voltage ramp range can be decreased further to have frequency scan bandwidths <30MHz which is appropriate for materials with small linewidths such as optical fiber. (b) Zoomed-in view of small frequency scan bandwidth on the signal analyzer. (c) Again, increasing the bias voltage of the voltage ramp sent to the VCO repositions the frequency scan range accordingly. The measured values acquired on the optical spectrum analyzer correspond to the optical beat frequency between the nominal laser frequency and the sidebands created by the frequency shifting EOM.

Small frequency scan ranges (<30MHz) can also be probed using small voltage ramps (<100mV), see Fig. 4.5. At 780nm, optical fiber has a Brillouin linewidth on the order of tens of MHz thus, for materials with small linewidths, we can change V_{tune} to probe small scan bandwidths. We demonstrated this in Fig. 4.5(a-b) by scanning V_{tune}

from 1.5 to 1.6V with a +2V bias. As with the wide scans, we can fine tune the scan range with the bias voltage to center our scan appropriately.

4.2.3 Pulse carving control

Both acousto-optic modulators (AOMs) and electro-optic modulators (EOMs) can be used to generate optical pulses. There are pros and cons to each; AOMs offer higher extinction but are often slower than EOMs which provide modest extinction but with shorter rise times. For these reasons and our application, we chose EOMs to generate ~ns pulses. Modulators being used for amplitude modulation, i.e. creating optical pulses, can be driven two ways: 'pulsed mode' or 'switching mode'. A schematic of these two modalities is shown in Fig. 4.6.

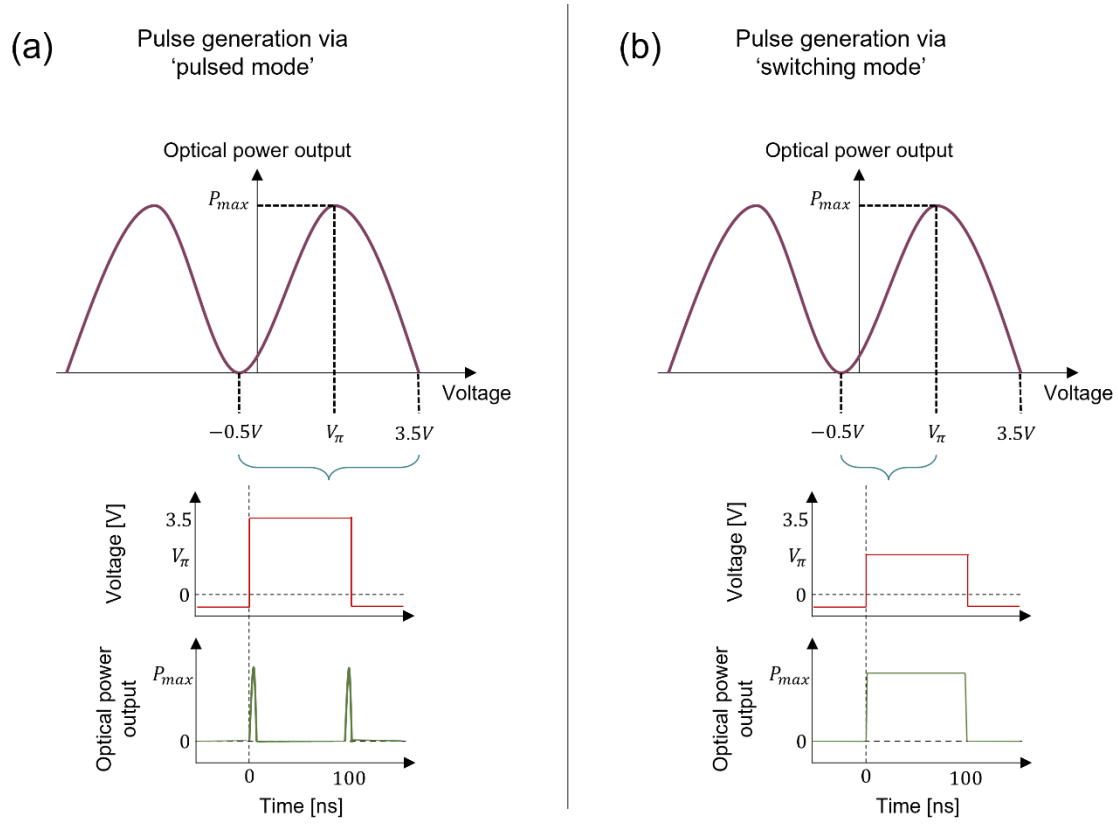

Fig. 4.6. Schematic of electrical control methodologies for generating pulses using EOMs. (a) Shows how short optical pulses can be generated via 'pulsed mode' operation. In this mode of operation, voltage is switched between two off-states ($-0.5V, 3.5V$ for simplicity) and an optical pulse (in green) is generated during the rise/fall time of the electrical signal (in red). The duration of said pulse is determined by the rise/fall time of the voltage signal. (b) Shows how optical pulses can be generated via 'switching mode' operation. In this mode of operation, voltage is switched between an off-state and an on-state ($-0.5V, V_\pi$ for simplicity) and an optical pulse (in green) is generated during the on-state time of the electrical signal (in red) which also determines the consequent pulse duration.

Running a modulator in pulsed mode entails driving the modulator between two consecutive voltages points of minimum optical power (V_0) also known as off-states. What this allows is for the modulator to reach the voltage point of maximum optical output (V_π), the on-state, during the rise time of the voltage signal. Subsequently, the resultant optical pulse has a duration according to the rise time of the voltage signal. This voltage associated with the maximum optical output is a critical specification for modulators as it determines the voltage signal needed in order to generate pulses with good modulation depth. This process also occurs during the fall time of the voltage signal thus the period of the pulses can be controlled in this manner. Pulsed mode is the optimal method for generating short pulses ($< ns$) as it relies on rise/fall times of the volage drive signal provided the modulator has a fast enough optical response. The EOMs we chose have a minimum optical rise time of ~200ps (Jenoptik, AM785) and ~500ps (Jenoptik, AM785b) respectively with a V_π of approximately 2V.

Another way to generate pulses is with switching mode where the voltage is driven between V_0 and V_π, i.e. an off-state and an on-state. In this mode, the optical output pulse reflects the duration of the voltage signal. For example, sending a 100ns RF voltage signal burst (with amplitude of V_π) creates a 100ns optical pulse. The period of the pulse can be controlled by the period of the voltage signal being sent.

Either modality of pulse generation can be biased accordingly to achieve the optimal modulation depth, i.e. peak optical output minus the minimum optical output power. Both modes are valid ways to generate pulses but the application (and desired pulse parameters) as well as the drive electronics (maximum voltage output and speed) should

be taken into consideration before choosing which mode to use. By changing our RF drive signal, we can control the pulse duration, period (and duty cycle), modulation depth, shape and number of pulses in a train.

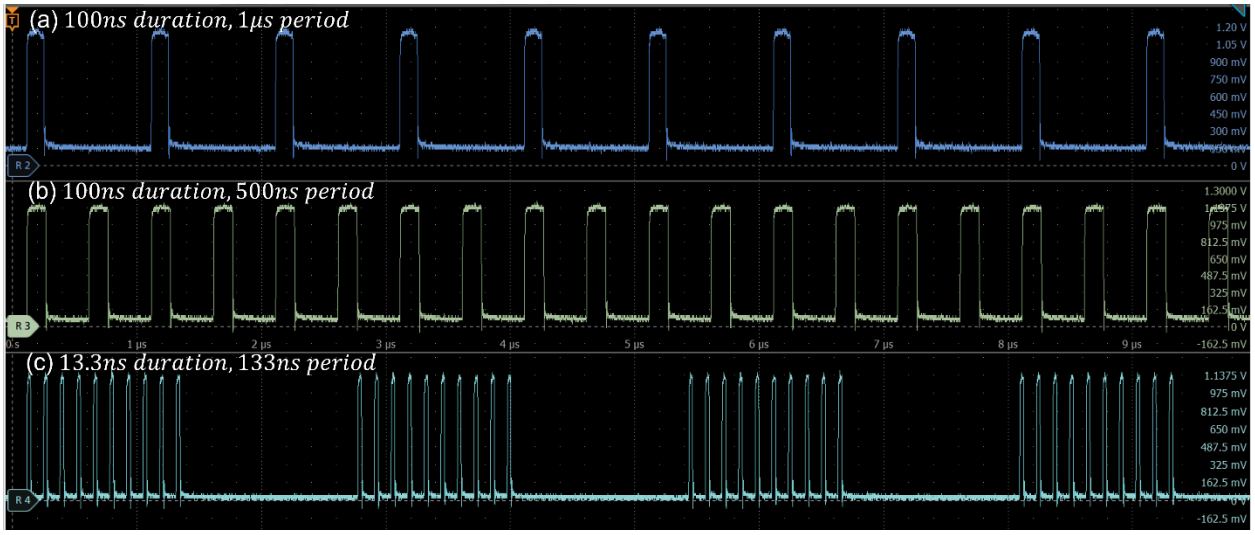

Fig. 4.7. Demonstration of pulse carving capabilities using the system described above. (a) Measured 10% duty cycle pulse train with 100ns pulse duration and 1μs period. (b) Measured 20% duty cycle pulse train with 100ns pulse duration and 500ns period. The 10μs segment shows how these trains could be synchronized to provide overlapping pulses for Brillouin interaction (sampled with 10 separate pulses) as well as having reference pulses (at twice the repetition frequency) to extract the Brillouin gain spectrum. (c) Measured example of short pulse generation at 10% duty cycle with a pulse duration of 13.3ns and 133ns period. A pulse train with 10 pulses such as these corresponds to a segment of 1.33μs which shows how faster measurement times are achieved using short pulses.

We performed a series of measurements using the pulsed SBS laser to demonstrate the control of the laser pulse parameters over different pulse durations and PRFs. First, we

created 100ns pulses with a 1μs period (10% duty cycle) by driving the pump arm EOM in switching mode. The RF voltage signal driving the EOM is repeated 10x in order to generate a 10 pulse long train of 10μs. The measured optical output is shown in Fig. 4.7(a). On the probe arm, the EOM is also driven in switching mode to create 100ns pulses but with a 500ns period (20% duty cycle) and is repeated 20x. The resultant probe pulse train is also 10μs long and is shown in Fig. 4.7(b). These two pulse trains represent what the respective pump and probe beams would look like for a 10μs frequency scan sampled at 10 steps across the frequency scan bandwidth. The overlapping pulses are for Brillouin interaction while also having reference probe pulses to calculate the gain spectrum. Furthermore, in Fig. 4.7(c), short pulse capabilities (13.3ns) at 10% duty cycle are demonstrated with a 133ns period. These pulses were generated with the pump EOM driven in switching mode. A 10 pulse long train with short pulses such as these result in an overall scan time of 1.33μs. When generating short pulses such as these, it is important to monitor the pulse train as the bias does need to be adjusted to ensure good modulation depth.

4.3 Conclusion

In summary, we have demonstrated the customizability of our pulsed SBS laser along with suggested optimal parameters for implementation into a Brillouin microscope setup. The MOPA architecture allows for reduced laser frequency noise due to the single seed laser of the design. We explained various considerations for the use of the laser and

how the frequency scan bandwidth can be tuned according to the needs of the user. The EOMs and their driving electronics were also addressed, and we showed how short pulses can be generated to create frequency swept trains for spectral acquisitions between 10μs and 1μs.

In order to be implemented into a microscope setup to measure biological samples, likely the receiver design should mirror the one described in Chapter 3 and leverage the polarization pulling effect to reach sufficient SNRs at such fast spectral acquisition times. In this way, the optimal power balance between the pump and probe arm can be used without saturating the detector.

Chapter 5: Summary of scientific contributions and future directions

5.1 Summary of scientific contributions

The results of my research have greatly influenced the measurement speeds of Brillouin microscopy. The use of Brillouin spectroscopy in the biological field has revolutionized the study of biomechanics and has allowed for the study of the mechanical properties of cells without perturbing or disturbing the sample; however, Brillouin microscopy has long been plagued with slow acquisition times which has kept it from becoming more prevalent in the field as a whole. Since the introduction of VIPA etalons, which have mostly replaced the use of FP etalons in Brillouin microscopy, spontaneous Brillouin microscopy has dominated the majority of research of biomechanics with respect to Brillouin spectroscopy, but due to the inefficient nature of the spontaneous Brillouin scattering process, there are few avenues for substantial speed improvements. That being said, the nonlinear counterpart to spontaneous Brillouin scattering, stimulated Brillouin scattering, has failed to become widely adopted despite the stronger possible Brillouin signals it has the potential to elicit. Continuous wave SBS was introduced to provide higher SNR and thus faster spectral acquisitions to the field of Brillouin microscopy but has only since made modest speed improvements due to nonoptimal power balances between the pump and probe beams and does not fully utilize the nonlinearity of the SBS process. Similar issues have recently been encountered in the few

attempts of implementing pulsed laser sources for SBS microscopy and suffer from the lack of proper laser sources with parameters suitable to Brillouin microscopy and suboptimal receiver designs to truly make an impact other than reducing average power delivered to the sample.

In Chapter 2, I implemented CW SBS in a flow cytometry setup to illustrate the first demonstration of high throughput biomechanical measurements with SBS. I characterized the system performance at 5ms spectral acquisition time, a 10x improvement over previous iterations of Brillouin flow cytometers. The throughput capabilities of the flow cytometer were accessed to have an overall throughput of 0.375 cells per second. The SBS flow cytometer was validated by measuring cell populations of normal breast epithelial cells and metastatic breast epithelial cells. Finally, I developed post-processing algorithms to analyze the Brillouin signatures of the cell lines. My first author publication of this work has been submitted.

In Chapter 3, I created an optimal receiver specifically designed for SBS spectroscopy based on polarization. All implementations of SBS microscopy, by nature of their design, suffer from the low-gain regime problem of trying to measure a small Brillouin gain signal riding on a very large background probe light level. First, I outline the issues associated with detector saturation limits and nonoptimal distribution of power between the pump and probe beams that have held SBS microscopy back from being truly competitive with spontaneous Brillouin systems. I proposed a model receiver design based on the polarization pulling effect which leverages the polarization dependence of the SBS interaction to effectively filter the signal from the background light. I developed

a noise model considering the various sources of noise and showed that the optimized receiver design could provide >25x SNR compared to standard SBS receivers in their typical experimental conditions. The experimental results of the receiver architecture enabled 100x higher SNR and thus enabled 100x faster measurements in the low-gain regime. Finally, I compared these results to current state-of-the-art SBS microscopy systems and discussed how this spectrometer design could benefit low-gain spectroscopy applications such as Brillouin microscopy. My first author publication of this work is in review in *APL Photonics*.

In Chapter 4, I took what I learned about fiber optics from Chapter 3 and applied that knowledge to build a proper customizable laser source specifically to be implemented into Brillouin microscopy. With its MOPA design, the separate pump and probe arms can be tuned and amplified according to the sample being tested, the desired measurement speeds, and power constraints. I characterized wide and small frequency scan bandwidths as well as pulse trains at 10μs and 1μs. This laser could be used in standard SBS detection or in polarization pulling SBS detection ports.

Overall, my research has resulted in two first author publications. I am also leaving the lab having built a laser system that will serve as the groundwork for many papers to come. During my time in the lab, I also was the Co-Entrepreneurial lead for a Brillouin Microscopy team for the National Science Foundation Innovation-Corps (NSF I-CORPS) regional and national programs; I presented in multiple capacities about the technology transfer of Brillouin microscopy in the field of ophthalmology / refractive

surgery diagnostics and conducted over 100 interviews with world-renowned refractive surgeons and industry leaders.

5.2 Future directions

While substantial speed improvements have been demonstrated with respect to source and detection optimization of SBS spectrometers in this work, there are still some additional modifications to be made to fully implement this technology for measurements of biological samples. The pulsed SBS laser currently built is capable of customizing the pulse parameters for optimal SBS measurements down to a spectral acquisition time of ~1μs. In order to be used in a microscope setup for biological measurements, i.e. in the low-gain regime, simply sending high peak power pulses at low duty cycles will not achieve the desired result of fast measurements; however, the combination of proper source and detection ought to be used in tandem. As I outlined in Chapter 3, optimal power balance between the pump and probe is necessary for high SNR Brillouin measurements while leveraging polarization-based receivers can circumvent the problem of detector saturation. Naturally, detector technology could advance in the future to have high saturation power fast photodetection, making the need for polarization-based detection obsolete, but until then this fact should be considered.

Furthermore, additional modifications to the pulsed SBS laser built in Chapter 4 could be made. I mentioned that EOMs could be driven in 'pulsed mode' and are most suitable for short optical pulse generation but do require higher RF voltage signals

compared to the 'switching mode'. An AWG with higher output voltage could be used to drive the EOMs in this mode as well as frequency sweep *in one step*, reducing the number of EOMs needed. This would cause a domino effect of benefits where having less EOMs would in turn cause less loss which would reduce how much amplification is done by the amplification stages and that would reduce amplified spontaneous emission noise and is something to consider moving forward. This concept was used in the system developed in Chapter 3, but such an AWG is extremely costly and the additional EOM / VCO drive was chosen as a result.

The next logical step following the research conducted in this thesis would be to explore the implementation of the pulsed laser system into a Brillouin microscope. The microscope setup presented in Chapter 2 would be an ideal platform to base this on with counterpropagating beams while modifying the detection to reflect the work completed in Chapter 3. Because of the need of counterpropagating beams, the likelihood of demonstrating pulsed SBS microscopy with flow cytometry at high throughputs or Brillouin images of in-vitro cells and spheroids are most probable. The measurement time chosen should be the time required to achieve 10MHz (or $1/30^{th}$ the linewidth of water) as was explored in Chapter 4 as well as completing an analysis of the thermal and ablative photodamage thresholds.

Another intriguing avenue to consider is the growing movement of commercial Brillouin which is something I learned from my experience during NSF I-CORPS. One company, Intelon, thus far has applied Brillouin microscopy (spontaneous) in the field of ophthalmology while two more, LightMachinery and CellSense, are looking into the

research market. However, the commercial landscape provides different challenges than in academic research labs. One clear instance of this is shown in the devices chosen for detection: spontaneous Brillouin in the academic research field (for optimal detection) uses expensive EMCCDs while commercial systems use cheaper photodetectors. This decision is motivated mainly by the need for a commercial system to be priced competitively with other diagnostic tools thus using cheaper detection methods lowers the cost-of-goods-sold (COGS). This commercial viability is still in its infancy for spontaneous Brillouin microscopy but is far more promising than stimulated Brillouin microscopy. Certainly, the overall complexity of SBS systems would prove significantly more expensive than spontaneous Brillouin, but additionally, the need of counterpropagating beams severely limits the number of applications that SBS could be used for. Take diagnostic tools for ophthalmology as an example where spontaneous Brillouin is quite promising as a way to measure corneal stiffness. It would be very challenging (or impossible) to imagine an architecture where SBS could be used in this application and as such, SBS microscopy is likely to be used nearly exclusively for flow cytometry biomechanical measurements and in-vitro Brillouin images. Thus, SBS conceivably could enter commercial relevancy in the research field for these aforementioned applications.

Bibliography

1. L. Brillouin, "Diffusion de la lumière et des rayons X par un corps transparent homogène: Influence de l'agitation thermique," Ann. Phys. **9**(17), 88–122 (1922).
2. E. Gross, "Change of Wave-length of Light due to Elastic Heat Waves at Scattering in Liquids," Nature **126**(3171), 201–202 (1930).
3. J. R. Sandercock, "Brillouin scattering study of SbSI using a double-passed, stabilised scanning interferometer," Optics Communications **2**(2), 73–76 (1970).
4. J. Randall and J. M. Vaughan, "The measurement and interpretation of Brillouin scattering in the lens of the eye," Proc. R. Soc. Lond. B. **214**(1197), 449–470 (1982).
5. J. M. Vaughan and J. T. Randall, "Brillouin scattering, density and elastic properties of the lens and cornea of the eye," Nature **284**(5755), 489–491 (1980).
6. G. Scarcelli and S. H. Yun, "Confocal Brillouin microscopy for three-dimensional mechanical imaging," Nature Photon **2**(1), 39–43 (2008).
7. M. Shirasaki, "Large angular dispersion by a virtually imaged phased array and its application to a wavelength demultiplexer," Opt. Lett. **21**(5), 366 (1996).
8. G. Scarcelli and S. H. Yun, "Multistage VIPA etalons for high-extinction parallel Brillouin spectroscopy," Opt. Express **19**(11), 10913 (2011).
9. G. Scarcelli, P. Kim, and S. H. Yun, "Cross-axis cascading of spectral dispersion," Opt. Lett. **33**(24), 2979 (2008).
10. G. Scarcelli, W. J. Polacheck, H. T. Nia, K. Patel, A. J. Grodzinsky, R. D. Kamm, and S. H. Yun, "Noncontact three-dimensional mapping of intracellular hydromechanical properties by Brillouin microscopy," Nat Methods **12**(12), 1132–1134 (2015).
11. G. Scarcelli, S. Besner, R. Pineda, P. Kalout, and S. H. Yun, "In Vivo Biomechanical Mapping of Normal and Keratoconus Corneas," JAMA Ophthalmol **133**(4), 480 (2015).
12. J. N. Webb, J. P. Su, and G. Scarcelli, "Mechanical outcome of accelerated corneal crosslinking evaluated by Brillouin microscopy," Journal of Cataract and Refractive Surgery **43**(11), 1458–1463 (2017).
13. C. Handler, G. Scarcelli, and J. Zhang, "Time-lapse mechanical imaging of neural tube closure in live embryo using Brillouin microscopy," Sci Rep **13**(1), 263 (2023).
14. J. Zhang, F. Alisafaei, M. Nikolić, X. A. Nou, H. Kim, V. B. Shenoy, and G. Scarcelli, "Nuclear Mechanics within Intact Cells Is Regulated by Cytoskeletal Network and Internal Nanostructures," Small **16**(18), 1907688 (2020).
15. M. Nikolić, G. Scarcelli, and K. Tanner, "Multimodal microscale mechanical mapping of cancer cells in complex microenvironments," Biophysical Journal **121**(19), 3586–3599 (2022).
16. J. Zhang and G. Scarcelli, "Mapping mechanical properties of biological materials via an add-on Brillouin module to confocal microscopes," Nat Protoc **16**(2), 1251–1275 (2021).

17. M. Nikolić and G. Scarcelli, "Long-term Brillouin imaging of live cells with reduced absorption-mediated damage at 660nm wavelength," Biomed. Opt. Express **10**(4), 1567 (2019).
18. P. Shao, A. M. Eltony, T. G. Seiler, B. Tavakol, R. Pineda, T. Koller, T. Seiler, and S.-H. Yun, "Spatially-resolved Brillouin spectroscopy reveals biomechanical abnormalities in mild to advanced keratoconus in vivo," Sci Rep **9**(1), 7467 (2019).
19. S. Wäldchen, J. Lehmann, T. Klein, S. Van De Linde, and M. Sauer, "Light-induced cell damage in live-cell super-resolution microscopy," Sci Rep **5**(1), 15348 (2015).
20. P. P. Laissue, R. A. Alghamdi, P. Tomancak, E. G. Reynaud, and H. Shroff, "Assessing phototoxicity in live fluorescence imaging," Nat Methods **14**(7), 657–661 (2017).
21. R. W. Boyd, *Nonlinear Optics*, 3rd ed. (Academic Press, 1992).
22. C. Li, *Nonlinear Optics* (Springer Singapore, 2017).
23. R. Y. Chiao, C. H. Townes, and B. P. Stoicheff, "Stimulated Brillouin Scattering and Coherent Generation of Intense Hypersonic Waves," Phys. Rev. Lett. **12**(21), 592–595 (1964).
24. K. O. Hill, D. C. Johnson, and B. S. Kawasaki, "cw generation of multiple Stokes and anti-Stokes Brillouin-shifted frequencies," Applied Physics Letters **29**(3), 185–187 (1976).
25. N. A. Olsson and J. P. Van Der Ziel, "Cancellation of fiber loss by semiconductor laser pumped Brillouin amplification at 1.5 μm," Applied Physics Letters **48**(20), 1329–1330 (1986).
26. J. Arnaud, "Enhancement of optical receiver sensitivities by amplification of the carrier," IEEE J. Quantum Electron. **4**(11), 893–899 (1968).
27. T. Kurashima, T. Horiguchi, and M. Tateda, "Distributed-temperature sensing using stimulated Brillouin scattering in optical silica fibers," Opt. Lett. **15**(18), 1038 (1990).
28. X. Bao, D. J. Webb, and D. A. Jackson, "32-km distributed temperature sensor based on Brillouin loss in an optical fiber," Opt. Lett. **18**(18), 1561 (1993).
29. C. Y. She, H. Moosm□ller, and G. C. Herring, "Coherent light scattering spectroscopy for supersonic flow measurements," Appl. Phys. B **46**(4), 283–297 (1988).
30. I. Remer and A. Bilenca, "Background-free Brillouin spectroscopy in scattering media at 780 nm via stimulated Brillouin scattering," Opt. Lett. **41**(5), 926 (2016).
31. I. Remer and A. Bilenca, "High-speed stimulated Brillouin scattering spectroscopy at 780 nm," APL Photonics **1**(6), 061301 (2016).
32. C. W. Ballmann, J. V. Thompson, A. J. Traverso, Z. Meng, M. O. Scully, and V. V. Yakovlev, "Stimulated Brillouin Scattering Microscopic Imaging," Sci Rep **5**(1), 18139 (2015).
33. G. Zanini and G. Scarcelli, "Localization-assisted stimulated Brillouin scattering spectroscopy," APL Photonics **7**(5), 056101 (2022).
34. I. Remer, R. Shaashoua, N. Shemesh, A. Ben-Zvi, and A. Bilenca, "High-sensitivity and high-specificity biomechanical imaging by stimulated Brillouin scattering microscopy," Nat Methods **17**(9), 913–916 (2020).

35. T. Horiguchi, K. Shimizu, T. Kurashima, M. Tateda, and Y. Koyamada, "Development of a distributed sensing technique using Brillouin scattering," J. Lightwave Technol. **13**(7), 1296–1302 (1995).
36. D. M. Chow, Z. Yang, M. A. Soto, and L. Thévenaz, "Distributed forward Brillouin sensor based on local light phase recovery," Nat Commun **9**(1), 2990 (2018).
37. J. B. Murray and B. Redding, "Suppressing non-local effects due to Doppler frequency shifts in dynamic Brillouin fiber sensors," Opt. Express **28**(8), 10760 (2020).
38. M. Santagiustina, S. Chin, N. Primerov, L. Ursini, and L. Thévenaz, "All-optical signal processing using dynamic Brillouin gratings," Sci Rep **3**(1), 1594 (2013).
39. D. Marpaung, B. Morrison, M. Pagani, R. Pant, D.-Y. Choi, B. Luther-Davies, S. J. Madden, and B. J. Eggleton, "Low-power, chip-based stimulated Brillouin scattering microwave photonic filter with ultrahigh selectivity," Optica **2**(2), 76 (2015).
40. D. M. Chow and S.-H. Yun, "Pulsed stimulated Brillouin microscopy," Opt. Express **31**(12), 19818 (2023).
41. F. Yang, C. Bevilacqua, S. Hambura, A. Neves, A. Gopalan, K. Watanabe, M. Govendir, M. Bernabeu, J. Ellenberg, A. Diz-Muñoz, S. Köhler, G. Rapti, M. Jechlinger, and R. Prevedel, *Pulsed Stimulated Brillouin Microscopy Enables High-Sensitivity Mechanical Imaging of Live and Fragile Biological Specimens* (Bioengineering, 2022).
42. R. J. Pelham and Y. Wang, "Cell locomotion and focal adhesions are regulated by substrate flexibility," Proc. Natl. Acad. Sci. U.S.A. **94**(25), 13661–13665 (1997).
43. C.-M. Lo, H.-B. Wang, M. Dembo, and Y. Wang, "Cell Movement Is Guided by the Rigidity of the Substrate," Biophysical Journal **79**(1), 144–152 (2000).
44. S. Huang and D. E. Ingber, "The structural and mechanical complexity of cell-growth control," Nat Cell Biol **1**(5), E131–E138 (1999).
45. M. Chiquet, "Regulation of extracellular matrix gene expression by mechanical stress," Matrix Biology **18**(5), 417–426 (1999).
46. S. Huang and D. E. Ingber, "Cell tension, matrix mechanics, and cancer development," Cancer Cell **8**(3), 175–176 (2005).
47. K. R. Levental, H. Yu, L. Kass, J. N. Lakins, M. Egeblad, J. T. Erler, S. F. T. Fong, K. Csiszar, A. Giaccia, W. Weninger, M. Yamauchi, D. L. Gasser, and V. M. Weaver, "Matrix Crosslinking Forces Tumor Progression by Enhancing Integrin Signaling," Cell **139**(5), 891–906 (2009).
48. K. Franze, "Atomic force microscopy and its contribution to understanding the development of the nervous system," Current Opinion in Genetics & Development **21**(5), 530–537 (2011).
49. R. M. Hochmuth, "Micropipette aspiration of living cells," Journal of Biomechanics **33**(1), 15–22 (2000).
50. B. Fabry, G. N. Maksym, J. P. Butler, M. Glogauer, D. Navajas, and J. J. Fredberg, "Scaling the Microrheology of Living Cells," Phys. Rev. Lett. **87**(14), 148102 (2001).
51. F. Serwane, A. Mongera, P. Rowghanian, D. A. Kealhofer, A. A. Lucio, Z. M. Hockenbery, and O. Campàs, "In vivo quantification of spatially varying mechanical properties in developing tissues," Nat Methods **14**(2), 181–186 (2017).

52. J. Guck and E. R. Chilvers, "Mechanics Meets Medicine," Sci. Transl. Med. **5**(212), (2013).
53. S. C. Hur, N. K. Henderson-MacLennan, E. R. B. McCabe, and D. Di Carlo, "Deformability-based cell classification and enrichment using inertial microfluidics," Lab Chip **11**(5), 912 (2011).
54. O. Otto, P. Rosendahl, A. Mietke, S. Golfier, C. Herold, D. Klaue, S. Girardo, S. Pagliara, A. Ekpenyong, A. Jacobi, M. Wobus, N. Töpfner, U. F. Keyser, J. Mansfeld, E. Fischer-Friedrich, and J. Guck, "Real-time deformability cytometry: on-the-fly cell mechanical phenotyping," Nat Methods **12**(3), 199–202 (2015).
55. C. L. Yankaskas, K. N. Thompson, C. D. Paul, M. I. Vitolo, P. Mistriotis, A. Mahendra, V. K. Bajpai, D. J. Shea, K. M. Manto, A. C. Chai, N. Varadarajan, A. Kontrogianni-Konstantopoulos, S. S. Martin, and K. Konstantopoulos, "A microfluidic assay for the quantification of the metastatic propensity of breast cancer specimens," Nat Biomed Eng **3**(6), 452–465 (2019).
56. J. Zhang, X. A. Nou, H. Kim, and G. Scarcelli, "Brillouin flow cytometry for label-free mechanical phenotyping of the nucleus," Lab Chip **17**(4), 663–670 (2017).
57. J. Guck, S. Schinkinger, B. Lincoln, F. Wottawah, S. Ebert, M. Romeyke, D. Lenz, H. M. Erickson, R. Ananthakrishnan, D. Mitchell, J. Käs, S. Ulvick, and C. Bilby, "Optical Deformability as an Inherent Cell Marker for Testing Malignant Transformation and Metastatic Competence," Biophysical Journal **88**(5), 3689–3698 (2005).
58. X. Mao, J. R. Waldeisen, and T. J. Huang, "“Microfluidic drifting”—implementing three-dimensional hydrodynamic focusing with a single-layer planar microfluidic device," Lab Chip **7**(10), 1260 (2007).
59. P. Paiè, F. Bragheri, R. M. Vazquez, and R. Osellame, "Straightforward 3D hydrodynamic focusing in femtosecond laser fabricated microfluidic channels," Lab Chip **14**(11), 1826–1833 (2014).
60. Y.-J. Chiu, S. H. Cho, Z. Mei, V. Lien, T.-F. Wu, and Y.-H. Lo, "Universally applicable three-dimensional hydrodynamic microfluidic flow focusing," Lab Chip **13**(9), 1803 (2013).
61. D. Huang, H. Wang, X. Wang, K. Guo, Z. Yuan, J. Chen, and Y. Chen, "Investigation of Optimal Coupling Velocities of the Sample and Sheath Flows for Hydrodynamic Focusing," JMSE **8**(8), 601 (2020).
62. T. Moragues, D. Arguijo, T. Beneyton, C. Modavi, K. Simutis, A. R. Abate, J.-C. Baret, A. J. deMello, D. Densmore, and A. D. Griffiths, "Droplet-based microfluidics," Nat Rev Methods Primers **3**(1), 32 (2023).
63. S. L. Anna, N. Bontoux, and H. A. Stone, "Formation of dispersions using “flow focusing” in microchannels," Applied Physics Letters **82**(3), 364–366 (2003).
64. L. Mazutis, J. Gilbert, W. L. Ung, D. A. Weitz, A. D. Griffiths, and J. A. Heyman, "Single-cell analysis and sorting using droplet-based microfluidics," Nat Protoc **8**(5), 870–891 (2013).
65. D. Thibault, P. A. Jensen, S. Wood, C. Qabar, S. Clark, M. G. Shainheit, R. R. Isberg, and T. Van Opijnen, "Droplet Tn-Seq combines microfluidics with Tn-Seq for identifying complex single-cell phenotypes," Nat Commun **10**(1), 5729 (2019).

66. V. Swaminathan, K. Mythreye, E. T. O'Brien, A. Berchuck, G. C. Blobe, and R. Superfine, "Mechanical Stiffness Grades Metastatic Potential in Patient Tumor Cells and in Cancer Cell Lines," Cancer Research **71**(15), 5075–5080 (2011).
67. D. Hartono, Y. Liu, P. L. Tan, X. Y. S. Then, L.-Y. L. Yung, and K.-M. Lim, "On-chip measurements of cell compressibility via acoustic radiation," Lab Chip **11**(23), 4072 (2011).
68. S. E. Cross, Y.-S. Jin, J. Tondre, R. Wong, J. Rao, and J. K. Gimzewski, "AFM-based analysis of human metastatic cancer cells," Nanotechnology **19**(38), 384003 (2008).
69. M. Nikkhah, J. S. Strobl, E. M. Schmelz, and M. Agah, "Evaluation of the influence of growth medium composition on cell elasticity," Journal of Biomechanics **44**(4), 762–766 (2011).
70. E. A. Corbin, F. Kong, C. T. Lim, W. P. King, and R. Bashir, "Biophysical properties of human breast cancer cells measured using silicon MEMS resonators and atomic force microscopy," Lab Chip **15**(3), 839–847 (2015).
71. U. Cavallaro and G. Christofori, "Cell adhesion and signalling by cadherins and Ig-CAMs in cancer," Nat Rev Cancer **4**(2), 118–132 (2004).
72. S. Byun, S. Son, D. Amodei, N. Cermak, J. Shaw, J. H. Kang, V. C. Hecht, M. M. Winslow, T. Jacks, P. Mallick, and S. R. Manalis, "Characterizing deformability and surface friction of cancer cells," Proc. Natl. Acad. Sci. U.S.A. **110**(19), 7580–7585 (2013).
73. M. Dessard, J.-B. Manneville, and J.-F. Berret, "Cytoplasmic Viscosity is a Potential Biomarker for Metastatic Breast Cancer Cells," (n.d.).
74. D.-P. Zhou, Y. Dong, L. Chen, and X. Bao, "Four-wave mixing analysis of Brillouin dynamic grating in a polarization-maintaining fiber: theory and experiment," Opt. Express **19**(21), 20785 (2011).
75. M. A. Soto and L. Thévenaz, "Modeling and evaluating the performance of Brillouin distributed optical fiber sensors," Opt. Express **21**(25), 31347 (2013).
76. H. Schmid, "How to use the FFT and Matlab's pwelch function for signal and noise simulations and measurements," http://www.schmid-werren.ch/hanspeter/publications/2012fftnoise.pdf.
77. G. Scarcelli, R. Pineda, and S. H. Yun, "Brillouin Optical Microscopy for Corneal Biomechanics," Invest. Ophthalmol. Vis. Sci. **53**(1), 185 (2012).
78. G. Scarcelli, P. Kim, and S. H. Yun, "In Vivo Measurement of Age-Related Stiffening in the Crystalline Lens by Brillouin Optical Microscopy," Biophysical Journal **101**(6), 1539–1545 (2011).
79. F. H. Loesel, M. H. Niemz, J. F. Bille, and T. Juhasz, "Laser-induced optical breakdown on hard and soft tissues and its dependence on the pulse duration: experiment and model," IEEE J. Quantum Electron. **32**(10), 1717–1722 (1996).
80. J. M. Dela Cruz, J. D. McMullen, R. M. Williams, and W. R. Zipfel, "Feasibility of using multiphoton excited tissue autofluorescence for in vivo human histopathology," Biomed. Opt. Express **1**(5), 1320 (2010).
81. A. Vogel and V. Venugopalan, "Mechanisms of Pulsed Laser Ablation of Biological Tissues," Chem. Rev. **103**(2), 577–644 (2003).

82. J. Zhang, M. Nikolic, K. Tanner, and G. Scarcelli, "Rapid biomechanical imaging at low irradiation level via dual line-scanning Brillouin microscopy," Nat Methods **20**(5), 677–681 (2023).